3-2020

Rapid Analysis of Plutonium Surrogate Material via Hand-Held Laser-Induced Breakdown Spectroscopy

Ashwin P. Rao

RAPID ANALYSIS OF PLUTONIUM SURROGATE MATERIAL VIA HAND-HELD LASER-INDUCED BREAKDOWN SPECTROSCOPY

THESIS

Ashwin P. Rao, Second Lieutenant, USAF

AFIT-ENP-MS-20-M-115

DEPARTMENT OF THE AIR FORCE
AIR UNIVERSITY

AIR FORCE INSTITUTE OF TECHNOLOGY

Wright-Patterson Air Force Base, Ohio

AFIT-ENP-MS-20-M-115

RAPID ANALYSIS OF PLUTONIUM SURROGATE MATERIAL VIA HAND-HELD LASER-INDUCED BREAKDOWN SPECTROSCOPY

THESIS

Presented to the Faculty

Department of Engineering Physics

Graduate School of Engineering and Management

Air Force Institute of Technology

Air University

Air Education and Training Command

in Partial Fulfillment of the Requirements for the

Degree of Master of Science in Nuclear Engineering

Ashwin P. Rao, B.S.E.

Second Lieutenant, USAF

March 2020

AFIT Graduate School of Engineering and Management
Thesis / Dissertation Committee Approval Signature Page

Designator Number: AFIT-ENP-MS-20-M-115

Title: RAPID ANALYSIS OF PLUTONIUM SURROGATE MATERIAL VIA HAND-HELD LASER-INDUCED BREAKDOWN SPECTRSCOPY

Student's Name and Rank: 2d Lt Ashwin P. Rao

Approved:

Committee Chair Signature	SHATTAN.MICHAEL.B.1020784071 Digitally signed by SHATTAN.MICHAEL.B.1020784071 Date: 2020.02.28 14:29:49 -05'00'	Date: Feb 28, 2020
Committee Member Signature	John David Auxier II Digitally signed by John David Auxier II Date: 2020.02.28 09:54:27 -07'00'	Date: Feb 28, 2(
Committee Member Signature	PATNAIK.ANIL.KUMAR.1362420810 Digitally signed by PATNAIK.ANIL.KUMAR.1362420810 Date: 2020.02.28 13:10:03 -05'00'	Date: Feb 28, 2(
Committee Member Signature		Date:
Committee Member Signature		Date:

For Dissertations Only

Dean's Acceptance		Date:

ADEDEJI B. BADIRU, Ph.D.
Dean, Graduate School of Engineering and Management

AFIT-ENP-MS-20-M-115

Abstract

This work investigated the capability of a portable LIBS device to detect and quantify dopants in plutonium surrogate alloys, specifically gallium, which is a common stabilizer used in plutonium alloys. The SciAps Z500-ER was utilized to collect spectral data from cerium-gallium alloys of varying gallium concentrations. Calibration models were built to process spectra from the Ce-Ga alloys and calculate gallium concentration from spectral emission intensities. Univariate and multivariate analysis techniques were used to determine limits of detection of different emission line ratios. Spatial mapping measurements were conducted to determine the device's ability to detect variations in gallium concentration on the surface of sample. Chemometric techniques were implemented to build predictive calibration models from the entire spectral data set. Partial least-squares regression was determined to produce the superior calibration model for predicting Ga content in a Ce-Ga alloy. The results demonstrated the SciAps Z500-ER can be coupled with advanced multivariate analytical routines to efficiently and rapidly provide quantitative analysis of impurities in plutonium surrogate metal. By using a handheld LIBS device in lieu of traditional mass spectrometry methods, the chemical analysis time can be reduced to mere seconds. This has direct applications for several national security applications including directly enabling Pu pit production teams to meet the 80 pit-per-year production goal outlined in the 2018 Nuclear Posture Review.

Acknowledgements

This work was possible due to a significant amount of effort put forth by my collaborators at various institutions which allowed me to conduct a thorough analysis of the capabilities of the Z500. First and foremost, I would like to thank Dr. Matt Cook of the Institute for Nuclear Security at the University of Tennessee for providing access to the cerium-gallium alloys and assisting me in the bulk of my data collection and measurements at UT. His help during my TDYs and continued collaboration was critical to my success. I would also like to thank Duncan Brocklehurst, who made the samples as part of his Master's thesis at UT. Howard Hall from the Department of Nuclear Engineering at UT served as PI on the cerium analysis project, and assisted in administration of this work. Several individuals from Los Alamos National Laboratory assisted my data processing efforts. I would like to thank Connor Travis (USNA), Christopher Johnson (USMA), Dung Vu and Dana Labotka for collaborating on the initial data collection using the hand-held device. Jessica Bishop provided instrumental assistance with the implementation of chemometric techniques in my data analysis, and I am extremely grateful for her knowledge of the subject. Lastly, I would like to thank my committee members; LTC Michael B. Shattan, Dr. Anil K. Patnaik, and Dr. John D. Auxier II for their support, knowledge, and aid in my Master's thesis endeavors.

Ashwin P. Rao

Table of Contents

Page

List of Figures

List of Tables

RAPID ANALYSIS OF PLUTONIUM SURROGATE MATERIAL VIA HAND-HELD LASER-INDUCED BREAKDOWN SPECTROSCOPY

1. Introduction

1.1 Motivation

Strategic nuclear deterrence has been the foundation of U.S. national security for decades. In the past few years, our adversaries around the globe have begun ramping up their nuclear capabilities by adding to their stockpiles and developing new technologies which pose threats to current U.S. deterrence posture. To secure U.S. national security and strategic interests, various ongoing efforts are in play to ensure the effectiveness and readiness of our nuclear triad and its deterrence capabilities. The 2018 Nuclear Posture Review (NPR) has outlined several initiatives to be pursued by the United States to ensure the effectiveness of the nuclear stockpile [1]. One of these initiatives mandates the capability to produce plutonium pits at a rate of 80 pits per year by 2030.

Improvements to the current analytical techniques used to conduct chemical composition analysis are being examined. Novel tools Dan techniques capable of quicker, more efficient metallurgical analysis are highly sought after to continue advancing the field. The development of a portable device capable of analyzing plutonium samples and providing rapid measurements of impurity concentrations would greatly benefit pit production efforts and improve upon existing analytical techniques.

This work details the experimental process which developed the analytical techniques and algorithms allowing a commercially available laser-induced breakdown

spectroscopy (LIBS) device quantitatively analyze a plutonium surrogate alloy. This chapter serves to provide a brief background and summary of the approach, limitations, and accomplishments for this research.

1.2 Background

LIBS has been used as a diagnostic technique for a wide variety of applications, and has proven to be a versatile analytical tool. Traditional LIBS setups on the laboratory scale have been used for combustion diagnostics to calculate fuel-to-air ratios, as well as plasma diagnostics for calculations of electron density and temperature in a variety of experimental proceedings [2–6]. Recently, LIBS has garnered the attention of scientists in the nuclear engineering community for a variety of nuclear applications.

Experimental proceedings by Bhatt *et. al.* using a traditional LIBS setup identified uranium lines from uranium trioxide in order to detect and quantify uranium concentrations [7]. Several additional studies have used LIBS to identify nuclear material in different chemical matrices, including geological deposits [8, 9], uranium ores [10, 11] and surrogate nuclear debris [12]. Other studies by Chinni *et. al.*, Sarkar *et. al.*, and Gaona *et. al.* validated the use of LIBS for various nuclear safeguard applications including IAEA swipe analysis, reprocessing activities and standoff detection [13–15]. The technique has been proven to generate reliable results, however the space and equipment traditionally required in these setups does not fit the constraints imposed on nuclear material analysis in the field or laboratory glovebox.

Recently, HH-LIBS systems have been developed and used widely for industrial purposes, such as the Z series HH-LIBS devices produced by SciAps [16]. The SciAps Z500 weighs only 6 pounds, and costs approximately $40,000 (USD) [17]; it is widely used in the metal scrapping industry. The commercial device contains libraries for a large span of elements and can conduct rapid, automated spectral emission analysis

to determine elemental concentrations in a sample. While the factory settings of the device do not allow it to conduct analysis of lanthanides or actinides, these libraries can be built and added to the device from experimental data. Recent work has proven that the Z500 can be used to accurately determine concentrations of uranyl flouride (UO_2F_6) in sand by using an algorithm which compares sample spectral data to experimentally determined calibration curves. This work proved the device could detect Uranium at a level of 250 parts per million from simulated on-site samples. [17]. Additionally, Manard *et. al.* proved this same device could be used for detection of rare earth metals in a uranium matrix [18].

The study of spectral emission lines of plutonium and plutonium surrogates for forensic identification purposes is much less developed. While data on lines from plutonium in a mixed actinide sample has been tabulated, no thorough studies have been conducted concerning spectral analysis of Pu alloys using a hand-held LIBS device [19]. The most common detection methods for Pu involve passive systems, such as gamma or neutron spectroscopy. These methods can detect and identify Pu to certain constraints, but a compact, portable HH-LIBS device could yield several improvements to the analytical process. Additionally, the size of the required equipment and time required for collection of significant data from these aforementioned spectroscopic techniques make them unsuitable for rapid *in-situ* analysis.

Quantitative analysis of plutonium is typically conducted in the laboratory environment using plasma spectroscopy techniques, such as Inductively coupled plasma - optical emission spectroscopy (ICP-OES). This technique uses plasma to excite a sample and measures light from the deexcitation of the sample atoms [20]. Recent work has demonstrated capability of ICP-OES to identify optical emissions of plutonium; spectral data gathered can be processed and deconvolved for quantitative analysis [21]. While results of high resolution ICP-OES experiments show promise

for quantitative analysis of plutonium alloys, the complex equipment requirements and sample preparation process leave a few areas of improvement open for investigation. In contrast, the HH-LIBS device can provide a compact, portable system for rapid spectral data gathering and provide elemental analysis. The simplicity of the system and depth of its commercial capabilities make it an ideal candidate for the purpose of plutonium/plutonium surrogate fabrication and impurity concentration measurement.

Cerium is a common chemical surrogate for plutonium, and is often used in experimental studies in place of plutonium since it is easier to access and handle [22]. Due to the two metals sharing similarities in chemical, physical, electrochemical, and metallurgical properties, studying cerium alloys can often yield valuable insights into the behavior of plutonium alloys [23, 24]. The spectral emission from alloys of this surrogate can provide an excellent starting point towards building spectral calibration models, tools, and analysis routines to be later applied to plutonium alloy analysis.

1.3 Problem

The task of identifying the presence of different elemental impurities in a Pu metal matrix and conducting rapid in-situ measurements can be done using LIBS. A HH-LIBS device can easily gather spectral data from a Pu sample, however commercially available devices possess neither the requisite libraries nor the processing software needed to conduct this quantitative nuclear material analysis. This research seeks to develop an algorithm to identify cerium and quantify gallium concentration in a Ce-Ga alloy which can be loaded onto the handheld device to bolster its quantitative analysis capabilities. By building such a program from experimentally gathered spectra, and building a comprehensive emission database, the HH-LIBS device could be used to immediately identify provide dopant concentration information in Pu sur-

rogate materials. The insights and results from this process can then be extended to analyze of plutonium alloys.

1.4 Hypothesis

This research is based on the hypothesis that different emission lines from cerium and gallium can be distinguished and used to develop calibration models relating spectral intensities to Ga content of a sample. The handheld device can be used to take raw spectra from Ce-Ga samples of varying Ga concentrations. An analytical algorithm can then be developed from this data to calculate Ga concentration from spectral peak information, by constructing a calibration curve or using different chemometric techniques to construct predictive models. The Ga concentration in an unknown sample can then be measured by taking a spectral measurement and comparing the emission intensity data to the experimentally calibrated models loaded onto the device.

1.5 Approach

The settings of the hand-held device are first optimized for spectral acquisition. Spectra of samples made of cerium and gallium oxides are taken to tabulate lines of both cerium and gallium. An initial calibration curve program is created for cerium-gallium alloys using the spectral emission intensities of standard sample alloys of Ga content ranging from 0 to 3 weight percent. Employing useful line ratios identified by the aforementioned univariate analysis, multivariate analysis techniques are used to build more complex models relating several spectral line intensity predictor ratios to the concentration. Each calibration model is analyzed and compared by calculating limits of detection and other statistical parameters related to the accuracy of the model.

1.6 Research Assumptions and Limitations

This study is primarily limited by the design of the Z500. The accuracy of the calibrations made using data collected from the device will depend largely on the resolution of the system. It is assumed that the system resolution of 0.1 nm is enough to resolve differences between the cerium and gallium emission lines to be used in quantitative sample analysis. Additionally, since the device used in this thesis was used previously to detect uranium compounds in sand, we assume the device has been properly maintained and cleaned so that contamination from these samples does not interfere with the data collection.

This study is also limited by the resources available in a laboratory setting and the quality of experimental samples used to build the analytical program. As the alloying process used to make the cerium chips was not perfect, the data acquisition process must be optimized to get the best average spectra representative of each sample. Due to the compressed timeline of this master's program, there may not be enough time for the creation of a completely new sample set for analysis.

Spectra of lanthanides and actinides are quite crowded, and chemometric techniques will need to be utilized in order to process the large number of emissions before making multivariate calibrations or predictive models. The accuracy of these models will be limited by the statistical methods used to transform the raw data, as many of these linear algebra based methods of dimensionality reduction lose information explaining the complete variance of the sample set. These predictive models must be created with enough components such that most of the variance of the original data set is explained.

Lastly, many diagnostic calculations from spectral emission data are dependent on the reliability of tabulated parameters for different emission lines, such as transition strengths and probabilities. This study assumes the accuracy of those values

tabulated in the NIST Atomic Spectra Database, but any errors in these values would carry through the calculations and affect the diagnostic measurements done to characterize the LIP from the recorded emissions.

1.7 Research Contributions

This research advanced the analytical capabilities of a commercial HH-LIBS device. Some of the more notable contributions adn advances are:

- **Validated capabilty of COTS HH-LIBS system for lanthanide analysis:** This study confirmed that a commericially available hand-held LIBS device is capable of elemental concentration analysis of cerium alloys, a novel result in this field.

- **Groundwork for future Pu alloy studies:** This research developed techniques which can be used to conduct rapid in-situ analysis of plutonium samples at various stages in the pit production process. This provides the DoE with a critically desired capability to assist in meeting the 80 pits per year mission [1].

- **Provided a novel technique to evaluate alloy production quality:** The surface Ga mapping study conducted in this work yielded valuable insight into potential flaws of annealing and manufacturing techniques used to produce the Ce-Ga alloys. This technique could be used to improve the alloy production process, and can be further applied for plutonium manufacturing studies.

2. Theory

The development of a HH-LIBS system capable of detecting and analyzing plutonium surrogates requires an understanding of evolution of laser-induced plasmas and their spectroscopic signature, and their use in material composition analysis. First, a summary of plasma spectroscopy and the theory behind LIBS are presented. A short comparison of alternative analytical spectroscopic methods are presented. The quantitative techniques used to extract suitable diagnostic information about the plasma and sample composition are analyzed. A brief discussion on plutonium chemistry is provided to understand the need to quantify impurities in plutonium alloys and the forensic application of this metric. All literature related to LIBS of plutonium and other actinides using the HH-LIBS to date are summarized, and methods of utilizing plutonium spectral data for nuclear forensic analysis are discussed. Finally, an overview of the function and capabilities of the HH-LIBS device is provided. Together, the information provided in the following sections allow for an understanding and interpretation of the results and conclusions made in Chapters 4 and 5.

2.1 Optical Emission Spectroscopy

A summary of the fundamental concepts behind laser ablation and plasma optical emission spectroscopy are provided. This conceptual understanding helps us identify the parameter domain for the plasma produced from laser ablation, which is used for quantitative composition analysis of the sample. When laser photons impact a target, deposit energy into the surface. This energy deposition excites the surface atoms and strips electrons from the electron shell, ionizing the surface and creating a plasma. Depicted in Fig. 1, the optical emission generated by a plasma is measured by directing the signal with a series of mirrors and lenses into a spectrometer. The

spectrometer disperses the light into its different wavelengths, which can be detected using a camera. The intensities of various wavelengths are recorded to obtain the LIBS spectrum. Strong spectral emissions characteristic of particular atoms in the ablated sample show up as peaks in the spectrum; analysis of these peaks can yield significant information about the sample itself.

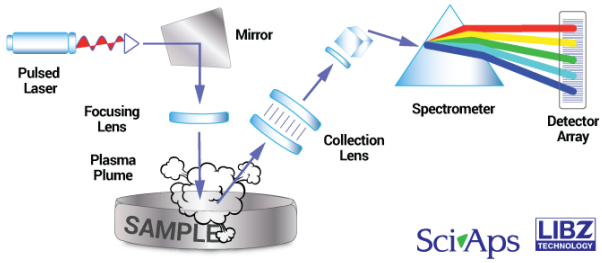

Figure 1. Schematic diagram of LIBS setup [16]. A pulsed laser ablates the sample surface; the recombination of particles in the resulting microplasma produces photons which can be captured by a spectrometer and recorded by a CCD camera. This spectra can then be analyzed to determine sample composition.

LIP spectral recordings can provide be used to determine the temperature and density of the plasma produced by the laser ablation event. The wavelength of different spectral lines can be matched to the emission wavelengths from a particular element to determine composition of the sample. The intensities of various lines in the spectra can then be used to determine the specific concentrations of different constituents of the sample itself. Overall, plasma spectroscopy is a valuable tool capable of providing a variety of information about a sample.

To understand how laser ablation of a sample can be utilized for chemical analysis, a discussion of the the theory behind laser induced breakdown is presented. This is followed by a basic overview of plasma spectroscopy. Finally, the techniques used to perform quantitative spectroscopic analysis are discussed in Sect. 2.1.2.

2.1.1 Laser Ablation

Laser ablation, depicted in Fig. 2, has traditionally been used to remove material from the surface of a target object. The ablation process itself occurs when short wavelength radiation from a laser beam couples with the material surface. The ablation process is fundamentally dependent on different laser parameters, including wavelength, pulse duration, repetition rate, and beam quality. Laser wavelength affects the energy of the laser photons, which determines the way in which they interact with the atomic matrix of the material. The type of coupling interaction is determined by the photon energy as described in Eq. 1.

$$E = \frac{hc}{\lambda} \tag{1}$$

Laser photons with energies higher than the atomic force attracting electrons to the nucleus will liberate these electrons from the atom, causing ablation. This process is defined as a "photochemical" interaction. Lower energy photons won't liberate electrons from their orbits, but will simply cause them to vibrate, causing molecular dissociations. If many such photons are incident on the atomic matrix of a material over time, the cumulative vibration is imparted as thermal energy. This interaction, called "photothermal" coupling, can also be used to remove electrons from the atomic matrix of a material [25].

Pulse duration and repetition rate affect the thermal characteristics of the ablation. Shorter pulses minimize thermal damage to the area surrounding the ablation event, and higher laser repetition rates enable maintaining a constant ablation temperature, preventing heat waste. Beam characteristics such as size, focus, and homogeneity are all factors affecting the ablation efficiency. These parameters must all be carefully evaluated prior to experimental data collection in order to perform successful ablation of a selected material.

Typically, ablation blows material off the surface of the target in the form of a gas. At higher laser fluxes, the ablated material interacts with a trailing portion of the laser pulse, further ionizing the ablated material. This ionization creates a plasma of the ablated surface material, forming what is referred to as a "laser-induced plasma".

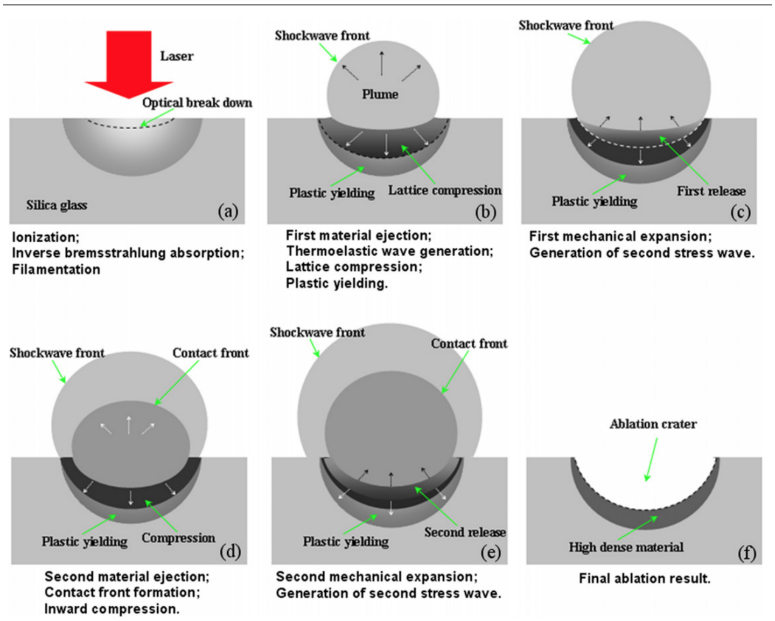

Figure 2. Breakdown of laser ablation process stages [26].

The general process of a laser ablation event is depicted in Fig. 2, describing the ablation of silica. Initially, the incident laser photons deposit part of their energy on the surface of the material, while part of the energy is absorbed through various ionization processes (multi-photon, inverse Brehmstrahlung, avalanche), creating the laser plasma. Next, material heated by the laser is ejected away from the target site. This heated mass transfers heat to the surrounding air, compressing it to create a shockwave front. Additionally, pressure induced by the laser forms a thermoelastic wave, which propagates as a pressure wave. This second stress wave further compresses material at the target site, leading to a second ejection and the formation of the contact front. As this front expands, further compression of the ablation site occurs and a third stress wave is generated. At the end of the ablation process, the

target site is left with an ablation crater filled with highly dense material formed from the compressions [26].

While this process occurs in the material, the plasma plume is expanding as a result of the shock front propagation. As it expands, the plasma begins to cool and recombine, leading to optical emission from various atomic shell transitions, which are discussed further in Sect. 2.2.1. The exponential temperature decrease is described in Fig. 3.

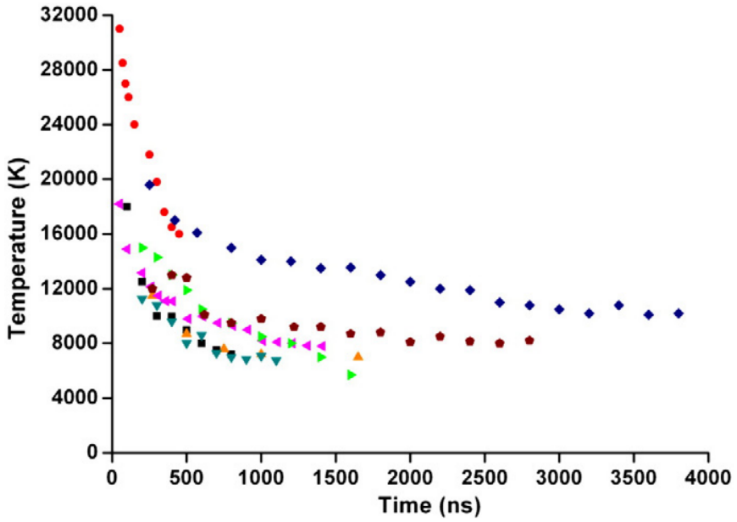

Figure 3. Example of temporal evolution of laser-induced plasma temperature [26].

As the ions and electrons recombine and the collision rate of the plasma slows, the temperature decreases to an asymptote over the period of a few thousand nanoseconds. Eventually, all the constituent particles of the plasma recombine.

In pulsed LIBS, the entire process described above is repeatedly cyclically between each laser pulse incident on the target material. For the purpose of material composition identification, a pulsed laser at a lower power and small beam diameter can be used to interrogate and collect data on a sample material with minimal damage beyond the ablation point on the surface.

2.1.2 Plasma Spectroscopy

Plasma spectroscopy describes a well established domain of optical emission analysis which involves recording the spectra of light emitted from a plasma for the purposes of quantitative analysis. The emission of spectral light occurs when an electron hole in an lower energy state of an ion is filled by atomic deexcitation. When an electron in a higher energy orbital transitions to a lower level electron hole, it releases a photon with energy corresponding to the difference in energy between the levels, as shown in Fig. 4.

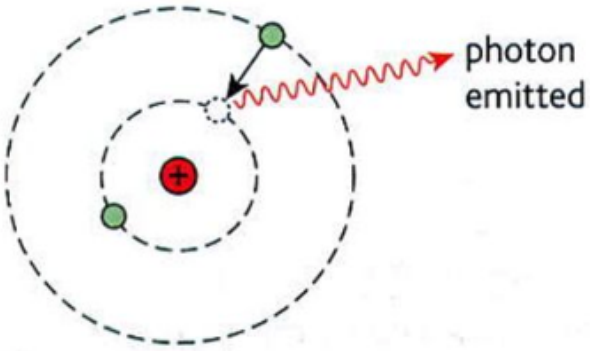

Figure 4. Basic rendering of the atomic de-excitation process.

De-excitation photon emissions from a plasma are characteristic of the specific energy level transitions of a particular atom. An example energy level diagram (ELD) is shown below for helium, along with different possible atomic transition paths. As evident from the figure, one element may emit photons at multiple wavelengths characteristic of one type of transition; some of these transitions are more probable than others.

Resonant transitions refer to transitions linked to the ground state; these transitions are favorable with high probabilities, and therefore the emitted radiation is generally intense. States which cannot decay via radiative transition are known as metastable, and have long lifetimes. Radiation in the visible spectra used for optical

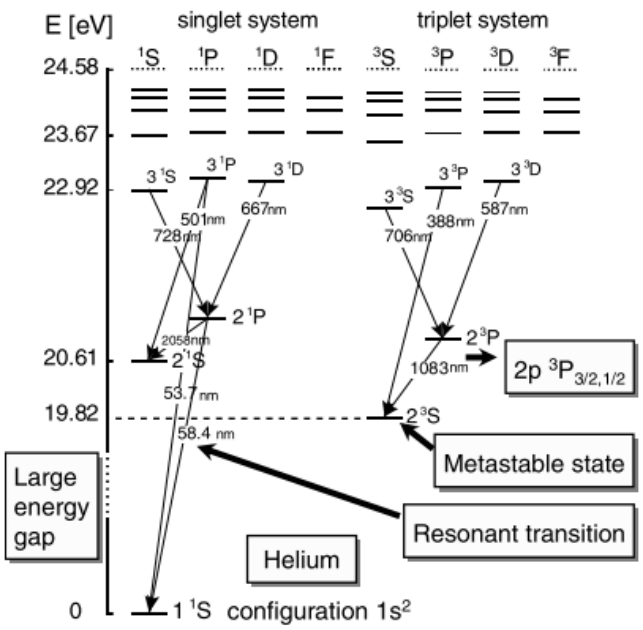

Figure 5. Atomic energy level diagram for Helium [27].

emission spectroscopy generally originates from transitions between different excited states [27]. The wavelength of the photon emitted from a transition can be calculated from the energies of the transition states as given in Eq. 2, where p is the initial level and k is the lower level.

$$\lambda_0 = \frac{hc}{E_p - E_k} \tag{2}$$

The intensity of the emitted light is a function of the particle density and the transition probability, and can be quantified as described in Eq. 3.

$$\epsilon_{pk} = n(p) A_{pk} \frac{hc}{4\pi\lambda_0} \tag{3}$$

The spectra of emitted light from a plasma can be recorded using a spectrometer. Emitted light directed into a spectrometer is collimated and focused onto a diffraction grating, which disperses the light into its different constituent wavelengths. The diffracted light is then reflected off a focusing mirror and can be directed onto a

detector, such as a CCD camera, to be recorded. The monochromator, shown in Fig. 6, is a commonly used spectrometer which can be coupled to a plasma experiment to record spectral emission of a particular narrow band of wavelengths. To record a larger bandwidth, some spectrometers do not use an exit slit, and instead direct all the diffracted light straight to a detector.

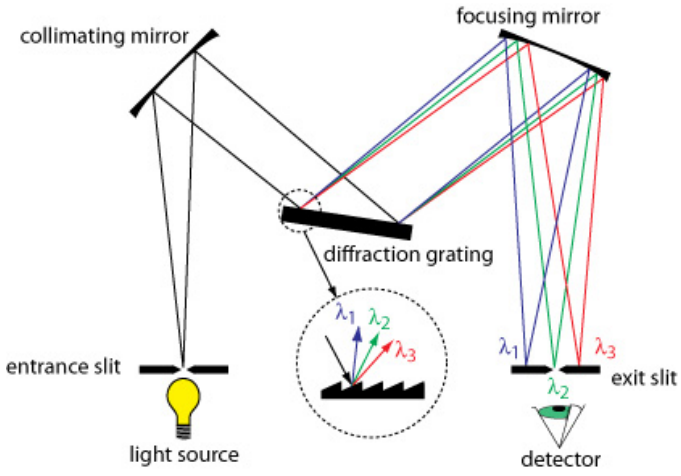

Figure 6. Schematic of Czerny-Turner style spectrometer.

With a "cold" light source, the emission lines read by the spectrometer would register as discrete lines at one single wavelength corresponding to one single energy level transition. However, the spectra from a plasma appear as broadened lines, or peaks, as seen in Fig. 7. The broadening of the spectral line by a plasma occurs due

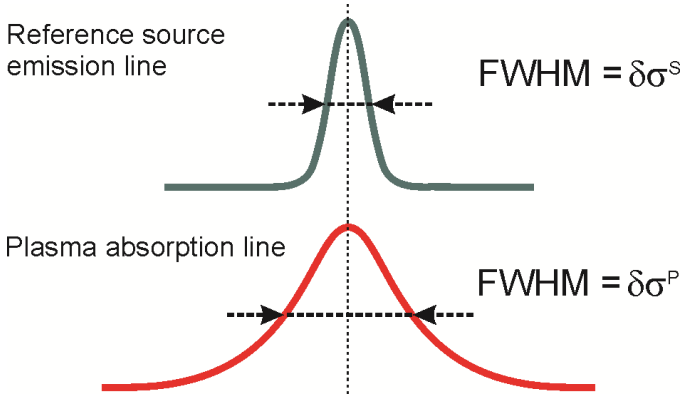

Figure 7. Depiction of spectral line broadening in plasma photon emission.

to the aggregate effects of several different phenomena in the plasma. The full width at half maximum (FWHM) of a broadened line can be approximated as follows

$$\Delta\lambda_{FWHM} = \sqrt{\Delta\lambda_D^2 + \Delta\lambda_S^2 + \Delta\lambda_A^2 + \Delta\lambda_{VDW}^2} \tag{4}$$

Eq. 4 equates the complete peak broadening as the sum of various broadening effects, including Doppler, Stark, apparatus/instrument, and Van-der-Waals broadening. In a plasma, two particularly important broadening mechanisms are Doppler and Stark. Doppler broadening stems from the velocity distribution of the particles in the plasma. Since every particle is emitted at a different velocity, each one has a different Doppler shift relative to the observer, causing a shift in the frequencies of emitted radiation. Due to the spread of velocities, there is variation in the Doppler shifts of the particles. This cumulative variation leads to Doppler peak broadening. Stark line broadening

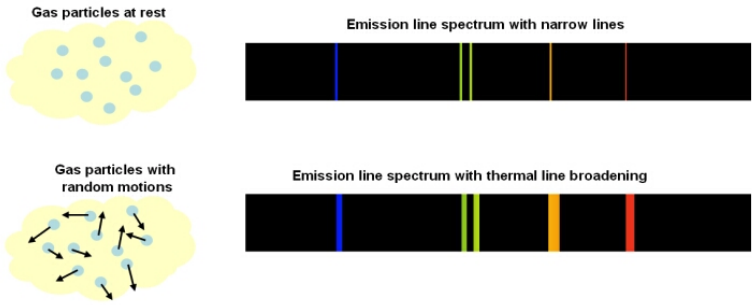

Figure 8. Depiction of Doppler line broadening effect.

occurs as a result of the Stark effect; the presence of an external electric field, such as the one created by the charged particle distributions inside a plasma, cause the splitting of degenerate energy levels in the atomic orbital. This is the electric field analog to Zeeman line splitting, and is demonstrated visually in Fig. 9. Splitting of the energy levels causes multiple photons at different wavelengths and intensities to be emitted for a given individual atomic energy state transition, broadening a discrete spectral line into a peak around the center wavelength of the transition. The line

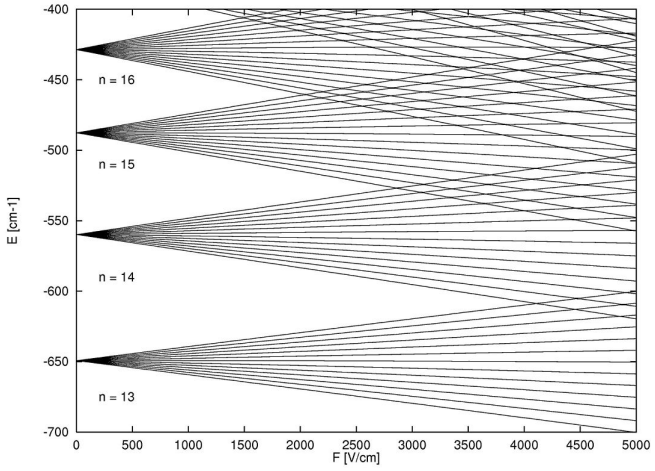

Figure 9. Stark line splitting of atomic energy levels caused by the presence of an external electric field.

broadening effects can be analyzed from recorded spectral data to provide diagnostic information about the laser plasma. The intensities of different lines in a spectrum can be used for quantitative calculations of sample composition.

2.2 Quantitative Spectral Analysis Techniques

Recorded spectral data can be processed and manipulated to provide diagnostic information of the electron temperature and density of the laser plasma. Intensity measurements of spectral lines can be compared to existing spectral data libraries to build calibration curves which can be utilized to determine isotopic composition of a sample. This section discusses the process of performing these calculations to conduct quantitative analysis of spectral data.

2.2.1 Electron Temperature Determination

Plasma temperature is a measure of the thermal kinetic energy of the particles in the plasma. Higher temperatures are required for a sustained ionization in the plasma,

and the degree of ionization itself is characterized by the electron temperature based on the Saha equation [28]:

$$\frac{n_{i+1}n_e}{n_i} = \frac{2}{\lambda^3}\frac{g_{i+1}}{g_i}\exp\left[-\frac{\epsilon_{i+1}-\epsilon_i}{k_B T}\right] \tag{5}$$

Electron temperature can be calculated from spectral line data assuming that the plasma satisfies the conditions for local thermodynamic equilibrium (LTE). If a plasma is in thermodynamic equilibrium (TE), the system can be described by a series of distribution laws, from which relations such as Eq. 5 are derived. Under this assumption, all the distributions for velocity, population, number density, and energy density can be characterized by the same unique temperature value. However, TE can never be achieved in a transient and inhomogeneous LIP; the radiative equilibrium demands that the plasma be optically thick at all photon frequencies, yet a LIP emits photons quite easily. As a result, the photon energy no longer obeys a Planckian distribution and TE is violated. However, if the energy loss due to photon emission is less than the energy required for other plasma processes (collisional ionization, photoionization, radiative decay, excitiation, Bremsstrahlung), the distributions governing population, number density, and velocity still apply [29]. These are the conditions which define LTE, and this can be quantitatively evaluated using the McWhirter criterion as seen in Eq. 6 [29, 30].

$$N_e > 1.6e12T^{.5}\Delta E_{nm}^3 \tag{6}$$

Using the McWhirter criterion to determine LTE, one can then use the Boltzmann plot method to determine electron temperature from spectral line data [4,6,29,31,32]. This method uses the following equation, derived from the Boltzmann distribution law. The values I_{nm}, λ_{nm}, A_{nm}, g_{nm}, and E_n refer to line intensity, transition wavelength, transition probability, degeneracy, and upper level transition energy. Intensity

and wavelength are taken from the spectral data, and the other values can be determined from tabulated data [33].

$$\ln \frac{I_{nm}\lambda_{nm}}{A_{nm}g_{nm}} = \frac{-E_n}{kT} + \ln \frac{hcN}{U(T)} \tag{7}$$

The left hand side of Eq. 7 can be plotted against the corresponding upper level energy for a given line. Multiple line values can be plotted together to generate a Boltzmann plot, as shown in Fig. 10. The electron temperature can be calculated as the negative reciprocal of the slope of the line fitted to the data points. The Boltzmann method of electron temperature calculation can be used to determine important diagnostic information about plasma temperature from a given set of recorded spectral data.

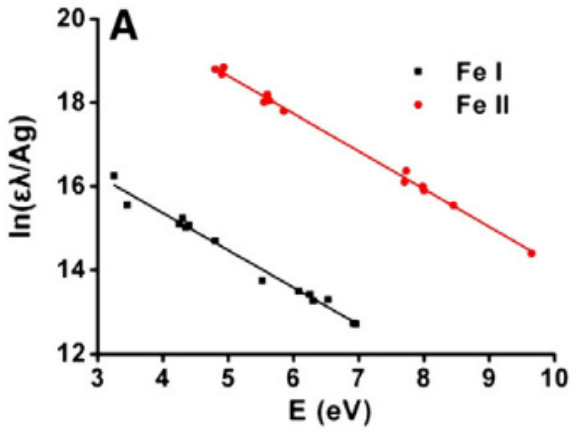

Figure 10. Example Boltzmann plot method using spectral data from Fe ionization lines as described in [29].

2.2.2 Electron Density Determination

Under the conditions of LTE described in the section above, we can assume that the LIP contains an equal number density of electrons and ion species. Electron density provides a measure of how many particles the plasma contains, and can be

used to evaluate other qualities of the plasma, such as optical thickness and RF attenuation. The electron density can be calculated from recorded spectral peaks by associating the electron density with peak broadening caused by the Stark effect, as mentioned in Sect. 2.3.2. The broadening of the peak due to the Stark effect is caused directly by the electric field created by the charge separation in the plasma. Changes in electron density affect this electric field, thereby affecting the extent to which a spectral line is broadened.

$$V(\lambda;\sigma,\gamma) = \int_{-\infty}^{\infty} G(\lambda';\sigma)L(\lambda-\lambda';\gamma)d\lambda \tag{8}$$

The line broadening from the Stark effect, called Stark broadening, can be determined by running a spectral peak through a mathematical processing routine. Assuming that Doppler and Stark broadening are dominant, any spectral peak can be approximated as the mathematical convolution of a Gaussian peak and a Lorentzian peak, corresponding to the Doppler and Stark broadened profiles, as shown in Eq. 8. This convolution is known as the Voigt profile fit (VPF). Here σ and γ refer to the Doppler and Stark broadening widths, respectively. Fig. 11 visually represents the results of a VPF and peak deconvolution routine of the LIBS spectra from the 566.6, 567.9 and 571.1 nm Nitrogen lines [34]. Using Stark widths extracted from the deconvolution, the following well-known equation can be used to calculate electron density [4, 31, 32, 35, 36].

$$N_e = \frac{\Delta\lambda_{1/2}}{2w}(10^{16}) \tag{9}$$

Here $\Delta\lambda_{1/2}$ refers to the Stark FWHM and w is a tabulated parameter known as fractional intensity width [28, 36, 37]. This method of spectral analysis is commonly used for electron density diagnostics of non-hydrogenic lines and is an efficient way of calculating this diagnostic parameter.

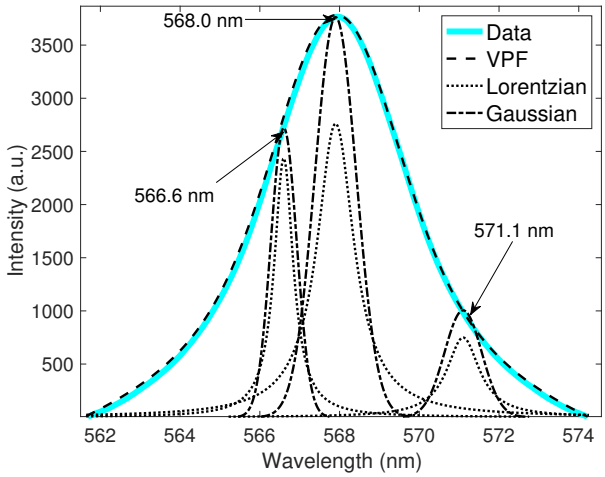

Figure 11. Example deconvolution of the N_{II} peak using a Voigt profile fitting routine [34].

2.2.3 Elemental Composition Determination

LIBS has demonstrated the ability to quickly determine elemental composition of a sample from spectral line intensity information [17, 38]. The intensity of a spectral line emission corresponding to a transition in a specific element is dependent upon the concentration of that element in a sample. As more atoms of the sample are present, more of these transitions can occur during laser ablation, and the line intensities will in turn increase. In a mixed-element sample, the ratio of intensities of two spectral lines corresponding to different constituent elements can be used to determine elemental concentrations. Data from an experimental sample can be compared to a calibration curve to identify and quantify concentrations of specific elements in the sample [17, 35, 39, 40]. Fig. 12 is an example of a calibration curve of lead concentration in brass standards built from LIBS spectral data. The intensity ratio scales linearly with concentration, forming a line which can be referenced to determine Pb concentration from spectral data of unknown samples. While this example reflects a high R^2 value of the calibration points, these data points can often have larger error bars as a result of shot-to-shot fluctuations of emission line intensities increasing the

standard deviation of the overall data set.

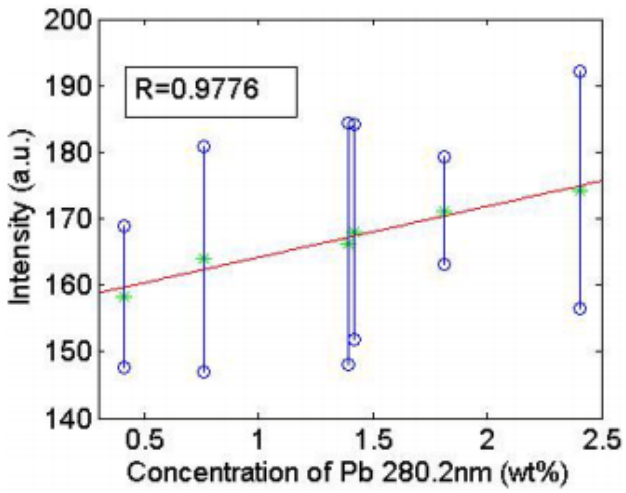

Figure 12. Example calibration curve from experimental data showing the increase in intensity ratio of Pb lines with increasing concentrations of lead in brass standard samples [38].

2.3 Alternate Material Composition Analysis Techniques

2.3.1 Inductively Coupled Plasma Optical Emission Spectroscopy (ICP-OES)

ICP techniques have long been used to quantitatively analyze sample composition and perform trace element analysis. ICP-OES is a destructive analytical technique which directs aerosol particles from a sample into an argon plasma and examines the spectral emission of the sample to determine its composition [41].

ICP-OES analysis is conducted by digesting sample material in nitric acid, and adding the solution to a peristaltic pump. The pump directs the solution into a nebulizer, which creates a fine aerosol out of the sample. The aerosol is then directed into an argon plasma to excite the molecules in the aerosol and induce ionization; the spectral emission is then recorded by a spectrometer and analyzed to determine

material composition [20].

While ICP-OES has been demonstrated to provided accurate elemental composition analysis, the size of the required equipment, lengthy sample preparation process, and time required to analyze a sample all make ICP-OES a non-ideal technique for a field analysis application [21]. Unlike ICP-OES, LIBS analysis can be conducted directly on a solid sample; no acid digestion is required. Additionally, while 12-15 mL of sample is required in ICP, LIBS can be conducted on much smaller sample areas due to the precision of the laser. Other differences between the two systems include the portability, compactness and shorter analysis time. All of these characteristics make the HH-LIBS device a more ideal candidate for detecting Pu in the field.

2.3.2 X-ray Fluorescence Spectroscopy (XRF)

In XRF, a sample is exposed to an x-ray photon source and is ionized; when an electron from a higher orbital falls into the place of an electron hole, another x-ray photon is emitted. This photon is then directed into a detector, which disperses the emitted photons based on either wavelength or energy. Different materials fluoresce at different wavelengths characteristic of their constituent atoms, and a spectra can be recorded to conduct elemental composition analysis of experimental data [42].

XRF is a common technique used in chemical analysis of various substances, and is similar to LIBS in efficiency, resolution, detection limits and time required for sample analysis. XRF also requires little to no sample preparation. Hand held XRF devices are commercially available, with detection speed and accuracy comparable to a HH-LIBS device [43].

However, for a portable, a handheld XRF is not ideal due to the fact that the system relies on a delicate, often expensive solid state detector. While XRF systems require these sensitive systems to detect light emission in the x-ray spectrum, LIBS

relies on visible and UV light, which can simply be passed through a robust transparent window into the spectrometer. This feature allows LIBS systems to be designed for use rougher conditions, as their ruggedness makes them much less prone to damage or failure. Additionally, XRF selectively excites certain atoms in a sample; this is dependent on the energy of the x-ray. For analysis of different elemental compositions, the x-ray has to be tuned to a different energy and a new set of measurements has to be conducted. This makes XRF inefficient for rapid, multi-element analysis. Since LIBS is characterized by ionization of the entire target volume, electronic de-excitation transitions from all constituent elements can be recorded. This allows for the analysis of multiple elements from one recorded spectra, making LIBS ideal for the application investigated in this work.

2.4 Plutonium Chemistry Overview

Plutonium is a critical material used in the manufacturing of "pits" of modern nuclear explosive devices. Plutonium is not naturally abundant, and must be produced in reactors through neutron absorption and decay by uranium. Common production pathways for Pu-239 and Pu-240 are shown below.

$$^{238}_{92}U +^{1}_{0} n \rightarrow^{239}_{92} U \rightarrow^{239}_{93} Np +^{0}_{-1} \beta + \bar{\nu} \begin{cases} \rightarrow^{239}_{94} Pu +^{0}_{-1} \beta + \bar{\nu} \\ +^{1}_{0}n \rightarrow^{240}_{93} Np + \gamma \rightarrow^{240}_{94} Pu +^{0}_{-1} \beta + \bar{\nu} \end{cases}$$

Pu-240 is also produced by (n,γ) reactions with Pu-239:

$$^{239}_{94}Pu +^{1}_{0} n \rightarrow^{240}_{94} Pu + \gamma$$

Upon recovery from reprocessed uranium, a variety of steps must be taken to form a weapon pit from the extracted plutonium, due to its complex material properties.

This section discusses the material properties and phase chemistry of plutonium, gives a description of events of interest in the pit production process, and discusses the properties of a common chemical surrogate for plutonium.

2.4.1 Pu Allotrope Chemistry

Plutonium metal exists in many different material phases, or allotropes, defined by different arrangements of the atoms in the crystal lattice of the metal. The mechanical and thermal properties of plutonium vary widely between the different phases; understanding the phase chemistry of Pu metal is critical to weapon core design and nuclear forensics. This particular property of plutonium makes it extremely sensitive to phases in temperature and allows for large changes in atomic volume between phase transitions [44]. Fig. 13 shows the change in atomic volume of plutonium with temperature, along with the various phase ranges and transition points. Upon ex-

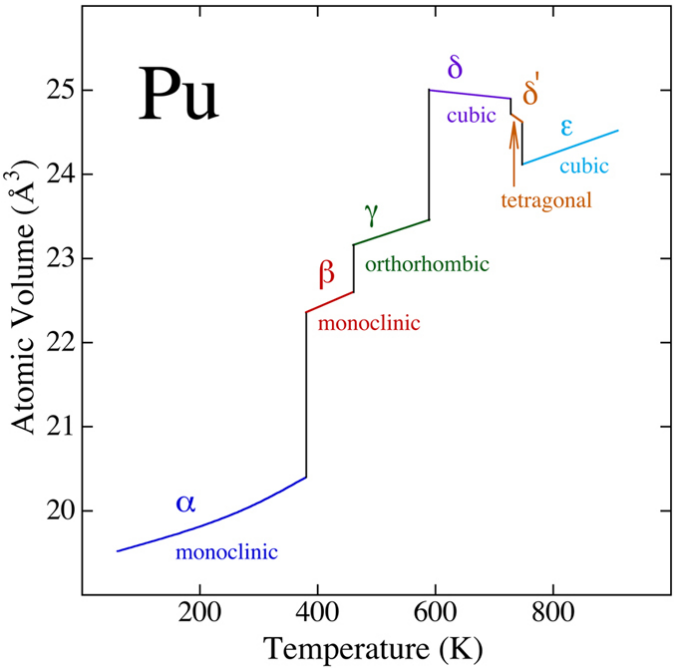

Figure 13. Atomic volume change over various temperatures for known Pu allotropes [44].

traction from reprocessed uranium fuel, plutonium is found in the alpha phase, which

exhibits a simple monoclinic crystal structure. As a result, it is brittle, weak and not easily compressed or machined. Additionally, it is susceptible to large changes in atomic volume over small temperature fluctuations. Both of these properties make it far from ideal for manufacture and use in a weapon pit. The beta (body-centered monoclinic) and gamma (face-centered orthorhombic) exhibit similar behavior as the alpha phase. The delta phase of plutonium can be reached by heating up Pu metal within 310 to 452 Celsius. This phase exhibits face-centered cubic (FCC) crystal structure, and is much less sensitive to volume changes due to temperature fluctuation. Additionally it behaves more like a traditional metal, and has a comparable strength and malleability to aluminum. Pu metal in this phase is easily machined and formed into weapon pits [45]. In order to stabilize delta phase Pu at room temperatures, the Pu metal must be heated and then alloyed with a dopant [45,46]. The most common alloying metal used is gallium. A phase diagram of Pu-Ga up to 12 atom percent Ga concentration is shown in Fig. 14. The phase diagram indicates that

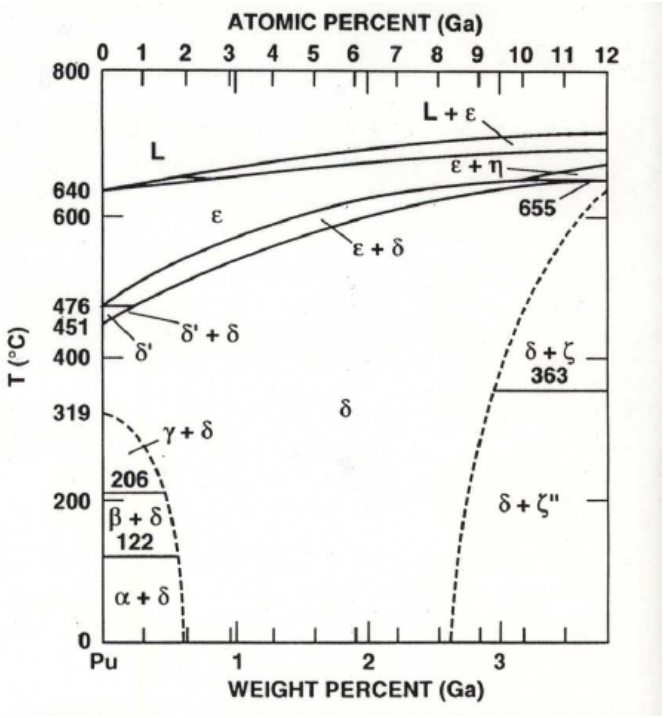

Figure 14. Pu-Ga alloy phase diagram [46].

alloying larger percentages of Ga with Pu allows for delta phase stabilization across a wider range of temperatures. This allows for the alloyed plutonium to be machined into the weapon pit upon cooling. An additional benefit to alloying plutonium with gallium is seen it its behavior in the weapon detonation process. Upon compression in a detonation, the Pu-Ga alloy pit will transition from the delta phase back to the denser alpha phase, helping reach supercriticality to kick-start the fission chain reaction. This property of the alloy is extremely important to the function of a nuclear device. Pu-Ga alloys are made by adding a certain amount of gallium to a mass of

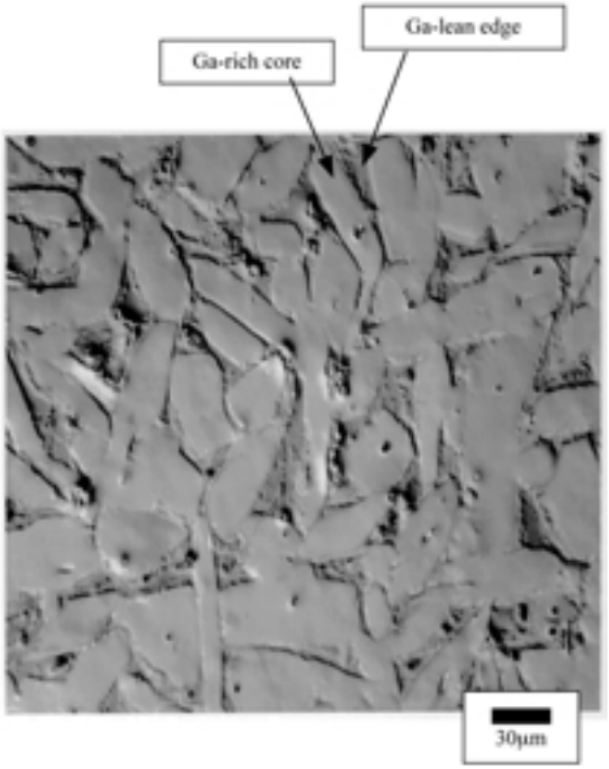

Figure 15. E-probe image of Pu-Ga alloy [24].

molten plutonium to achieve the desired weight percent of Ga. Gallium segregates itself in plutonium, forming rich grain centers and lean grain boundaries, as shown in Fig. 15. In order to diffuse the gallium through the plutonium, the alloy must be annealed at a temperature in the delta phase transition region. This homogenization

process stabilizes the lattice structure of the alloy. Upon cooling, the alloy stabilizes in the FCC configuration of delta-phase Pu, making it ideal for machining into a weapon pit [45].

2.4.2 Cerium as a Plutonium Surrogate

While conducting experimental LIBS measurements of plutonium alloys can yield valuable data, plutonium is relatively hard to access compared to other radioisotopes. However, conducting LIBS measurements of similar metals can provide more easily accessible results and help characterize the possible LIBS signatures of an actual Pu-Ga alloy. Cerium, a lanthanide metal, is a commonly used chemical surrogate for plutonium [22, 23]. Fundamental links between cerium and plutonium have been reported in several studies. Both metals have low melting points, asymmetrical crystal lattice structures, and multiple allotropes which exhibit large volume changes with phase transformations. The similarities in properties has been attributed to the face that f-shell electrons in both elements are in transition to a localized state [24]. Fig. 16 shows the E-probe image of a Ce-Ga alloy; this alloy exhibits the same

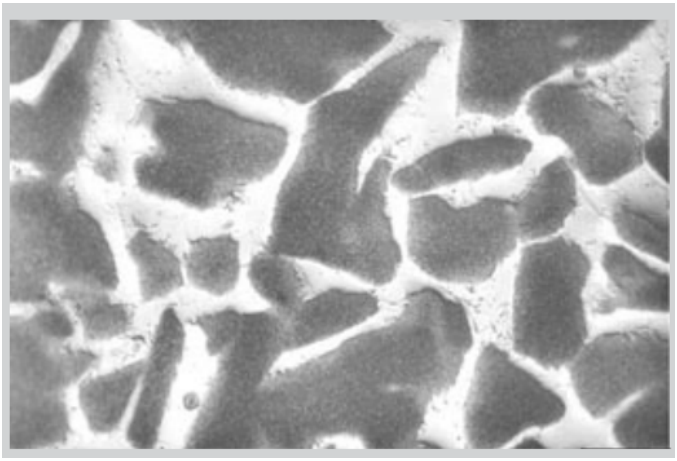

Figure 16. E-probe image of Ce-Ga alloy [24].

segregation behavior as seen in Pu-Ga in Fig. 15. The similarities between cerium

and plutonium have made cerium compounds a popular choice for use in experimental work to overcome many of the laboratory hazards of working with plutonium. Cerium compounds such as cerium oxides have been studied extensively as an experimental substitute for plutonium oxides, and the comparative behavior of both compounds in different experimental conditions has been documented in literature [22–24, 47]. This work will examine LIBS spectra of both Ce-Ga in metal and oxide forms and develop a base of analytical measurements which can be extended to Pu-Ga alloys.

2.5 LIBS for Nuclear Forensics

LIBS is an emerging technique of interest in the nuclear forensics community. Several studies have demonstrated the ability of LIBS to detect nuclear material in matrices relevant to the nuclear community, such as geological deposits [8,9], uranium ores [10,11], and surrogate nuclear debris [12]. Other studies validated the use of LIBS in nuclear safeguard applications, including analysis of IAEA swipe samples [13], nuclear reprocessing plant activities [14], and standoff detection of radiological threat materials [15]. LIBS has also been used to tabulate spectral lines of several actinide elements [19]. While traditional laboratory setups can provide rapid and accurate analysis of samples, the capabilities of portable handheld devices for field use still need to be thoroughly evaluated. Studies have been conducted using the HH-LIBS device used in this thesis work, in which the device was used to detect uranium compounds or anomalies in a bulk uranium matrix. These early results are promising, as they indicate that the Z500 can detect emissions of dopant elements in an bulk actinide matrix, despite the lower resolution of the device. This section discusses these studies in detail and their implications for quantitative analysis of cerium-gallium alloys using the HH-LIBS device.

2.5.1 HH-LIBS for Nuclear Forensic Analysis

Previous work using the Z500-ER has confirmed uranium detection capabilities of the hand held device. This work examined spectra of uranyl flouride (UO_2F_2), which was mixed with sand to produce samples varying from 1 to 39.5 weight percent UO_2F_2 [17]. Fig. 17 shows the variation in the spectra of the 409.1 U(II) peak height

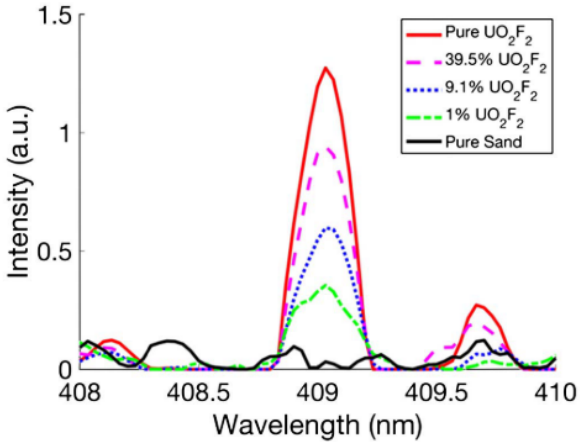

Figure 17. U(II) 409.1 nm peak for varying uranyl fluoride concentrations [17].

over different concentrations. It is expected that as the uranium concentration in the sample decreases, the line intensity decreases since less of the transitions emitting the 409.1 nm line are occurring. Calibration curves were built using intensities of each uranium line selected for all sample concentrations, an example calibration curve for the U II 409.1 nm line is shown in Fig. 18. The fitted line to the datapoints gives the calibration curve which can be used to determine concentration of an unknown sample once the appropriate line ratios has been calculated. This technique can be applied to Ce-Ga alloys as well, allowing the creation of a calibration curve for the plutonium surrogate.

An additional study conducted by Manard et. al. [18] demonstrates how the Z500 can be used to discriminate rare earth metals in a uranium matrix. Here, the Z500 was able to detect Eu, Nd, and Yb in levels up to hundredths of a percent in a

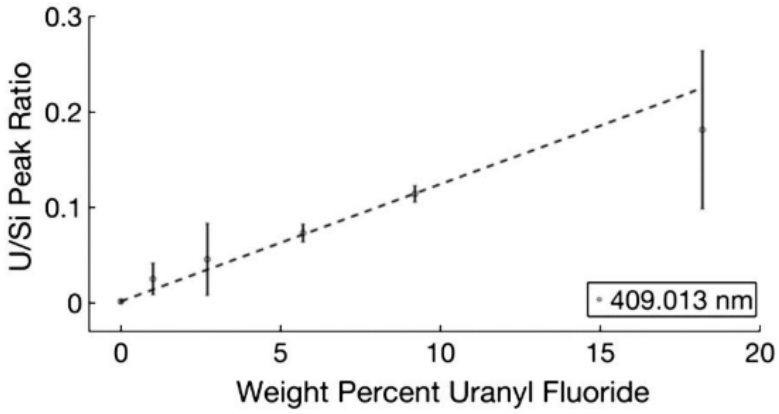

Figure 18. Calibration curve for the U II 409.1 nm line [17].

uranium oxide powder. These results indicate that the HH-LIBS device is capable of detecting dopants in a bulk actinide compound matrix and also show promising potential for the Z500 device to discriminate and identify gallium in a cerium, or even plutonium matrix.

Finally, recent work conducted at LANL using the SciAps Z300, a similar HH-LIBS device, confirms that these devices can be used to analyze surrogate nuclear melt glass [48]. The chemometric techniques used to bolster the analytical capabilities of the Z300 in the study can be applied to the quantitative analysis of cerium alloys in this work as well. The experimental methodology used in the works discussed above will be applied to this thesis to record, select, and analyze emission lines of cerium and gallium to perform quantitative analysis of these materials.

2.6 Chemometrics

The univariate calibration curve analysis method described in Sect. 2.2 is a simple technique useful for detection and elemental composition determination from relatively uncluttered spectral data. However, when dealing with spectra of heavy metals and high Z elements, the large number of possible atomic transitions leads to a much

more crowded emission spectra with a large amount of data to sort through in order to begin any form of quantitative analysis. Chemometrics refers to a set of statistical and mathematical techniques used to simplify and process large sets of chemical data. The goal of applying chemometrics is to determine patterns and correlations from the extracted data in order to build models describing variations in the data set to properties of the samples. Chemometrics employs multivariate statistical analysis techniques, used to simplify large data sets and find relations between different dependent variables influencing an outcome variable. Multivariate analysis is especially useful in processing LIBS data, due to the complex nature of spectral responses and the large number of variables present [49–54]. This section describes different multivariate analysis techniques which were utilized in this thesis work to analyze the complex cerium alloy spectra.

2.6.1 Multivariate Regression

Multivariate regression can be used to construct a single regression model based on multiple different predictor variables [55–57]. Compared to simpler linear regression, multiple regression models provide better precision for estimation and prediction of outcome estimates, such as elemental concentration. A simple multivariate regression model can express an outcome as a function of two independent predictor variables by extrapolating the regression line to a 3D plane, shown in Fig. 19. This regression plane is given by the equation

$$y = \beta_0 + \beta_1 x_1 + \beta_2 x_2 \tag{10}$$

Here, the beta coefficients correspond to slopes of the independent variables. x_1 and x_2 correspond to the values of the x and z axes in Fig. 19. This model is the genesis of the multivariate regression. Multiple independent predictor variables can be included

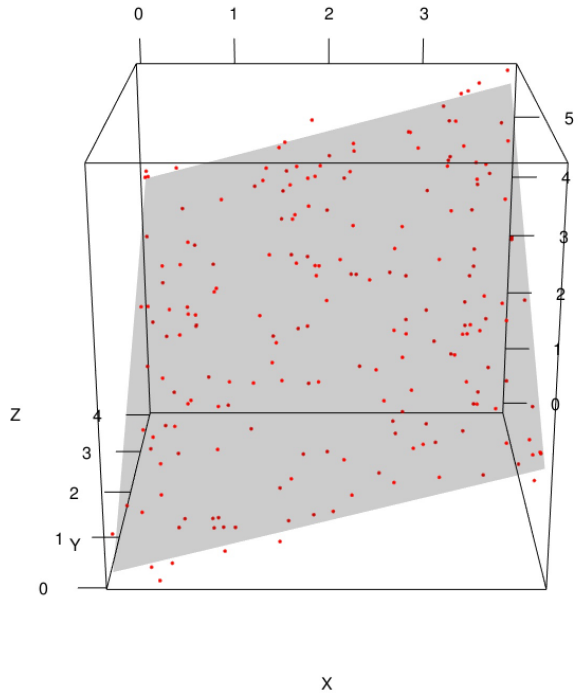

Figure 19. 3D multivariate regression plane. [56].

in the model, with each variable having a slope term in the regression equation, which can be extended as follows:

$$y = \beta_0 + \beta_1 x_1 + \beta_2 x_2 + ... + \beta_n x_n \tag{11}$$

Eq. 11 can be applied to spectral data in order to generate a multivariate model relating elemental concentration to the intensity or intensity ratio of multiple spectral lines in the data set. This multivariate calibration model can yield more accurate determinations of elemental concentration with lower limits of detection than a univariate calibration can, making it a simple but valuable technique in more complex analysis of spectral emission data [53].

2.6.2 Principle Components Analysis (PCA)

PCA is a statistical analysis technique used to reduce the dimensionality of a complex data set by creating a smaller set of variables describing the variance in most of the original data [55,58]. PCA algorithms are commonly used in the LIBS community to identify significantly varying spectral lines in crowded spectral data sets and analyze only the factors causing variations in the data [9,50–54,57,59]. PCA uses matrix algebra to construct linear combinations of the original data set variables, called principle components (PCs). Each PC is uncorrelated, but most of the information in the data set is compressed into the first few PCs. Each component explains a percentage of the total variance of the overall data set; this can be graphically represented in order to determine how many PCs are needed to represent the data set. An example is shown in Fig. 20. PCA outputs two information matrices for each PC: loadings

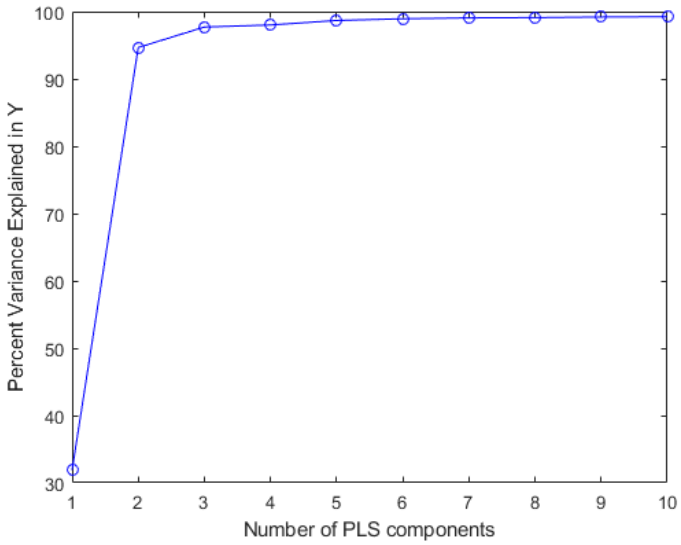

Figure 20. Percent of explained variance in data set vs. principle component number.

and scores. Loadings describe correlations between the variables, as well as their relative contributions to the data set. Scores quantify patterns and correlations between samples in the data set itself. Examining the relationship between loadings values

and emission wavelengths of LIBS spectra can identify the emission lines causing the most variance in the data set, and aid in variable reduction. An example is given in Fig. 21.

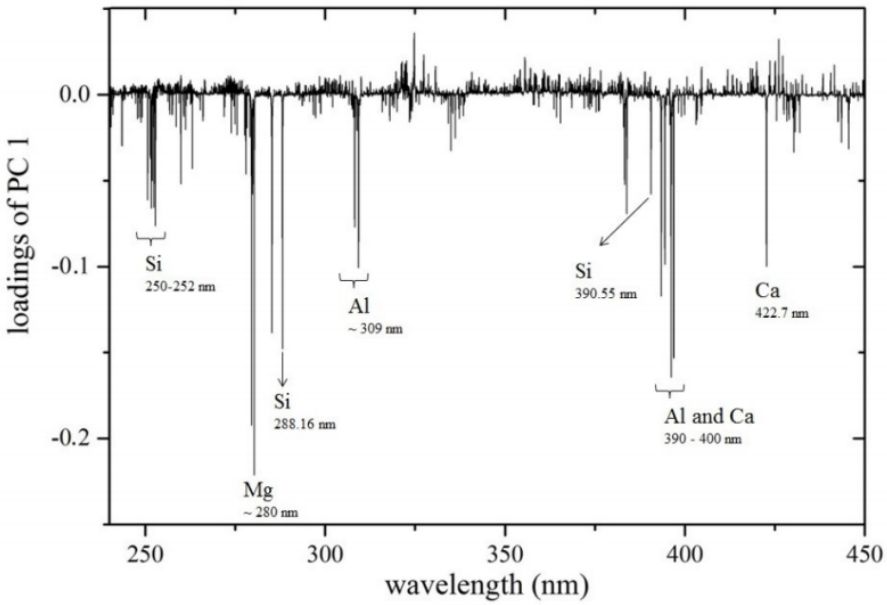

Figure 21. Example PC loadings of LIBS spectra. Significantly varying emission lines in the data set are clearly identified by their loadings values [59].

This loading plot identifies emission lines which vary the most among different samples in the spectral data set. By identifying these wavelengths, the data set can be reduced to look solely at these variables, greatly simplifying the original cluttered spectra. Running a PCA algorithm on the simplified variable set allows for further grouping and analysis of the similarities between the LIBS spectra of the samples. For example, comparing the loading values of different principle components can cluster the variables by element, as seen in Fig. 22. These example loadings plots discriminate the variables based on element of emission origin, and quantify the influence of individual spectral lines to the discrimination of the sample.

PC scores can further aid in clustering samples in the data sets based on quantified similarities. Fig. 23 schematically describes the sorting of different samples by

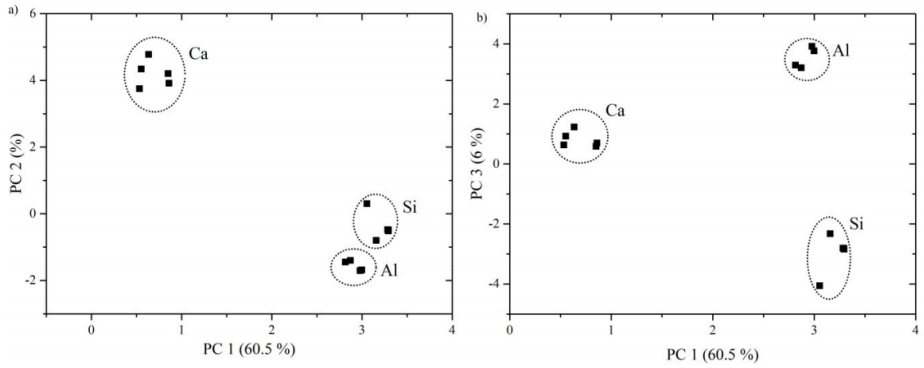

Figure 22. Example of comparative plot of different PC loadings from a LIBS data set. The loadings clearly cluster variables based on elements from which certain atomic emissions manifested [59].

chemical matrix type based on the relationship between scores of different PCs. This

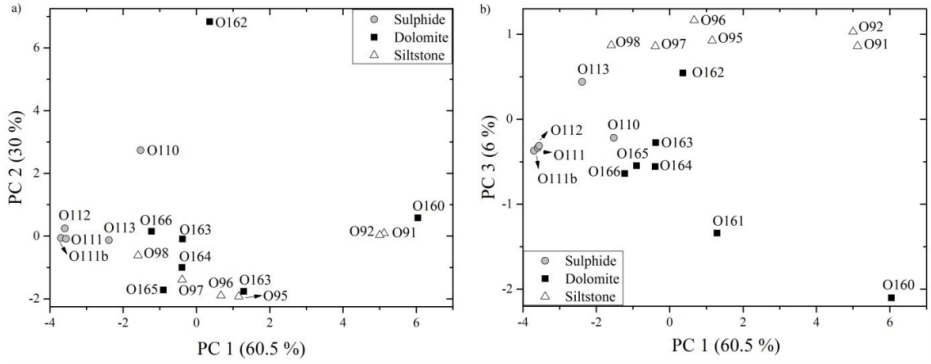

Figure 23. Example PC scores of LIBS spectra. Scores help identify patterns between the samples in the data set, such as sample type or elemental concentration [59].

technique is particularly useful in the LIBS community for discrimination of samples based on a particular property or criterion of interest. This allows for the sorting of samples based on matrix type, or dopant concentration levels, which is particularly useful in nuclear forensic applications. Overall, PCA is a powerful tool for spectroscopic analysis which can greatly aid in the clustering of complex spectral data and the identification of elements of interest within a sample set.

A regression model can be formulated using outputs of a PCA calculation; this is known as principle components regression (PCR). Regression coefficients relating the

response variables to the predictor data (principle components) can be calculated by conducting a linear regression between the mean deviations of the response variables and the scores of the desired PCs. These coefficients can then be multiplied by the original spectral data variables to create a regression fit model relating the PC scores to the outcome. In doing so, a predictive model can be generated to determine elemental concentration from a set of spectral data using the outputs of a PCA algorithm.

2.6.3 Partial Least Squares Regression (PLSR)

PLS regression is a technique which combines features from ordinary multivariate regression and PCA, and is another commonly used technique used to analyze complex LIBS spectra of a limited sample set [8,54,57,60,61]. A PLS regression builds a model predicting an outcome from predictor variables in order to describe their common structure. PLSR finds a set of components called latent vectors, which decompose the predictor and outcome matrices such that the information contained within the latent vectors explains as much of the variance between the predictors and outcomes as possible. A regression then decomposes the predictor matrix in order to determine outcome.

At the simplest level, PLS analysis involves generating a regression model which correlates the LIBS spectral data (X) to elemental concentrations (Y) as described in Eq. 12.

$$Y = XB \tag{12}$$

B represents a regression coefficients matrix describing the relationships between the spectral emission intensities and the elemental concentrations (response). Comparing the regression coefficients to the predictor variables (wavelengths) generates a plot similar to the loadings comparison depicted in Fig. 21. This allows for discrimination

of the important variables in the data set, as noted in Fig. 24. The PLS algorithm

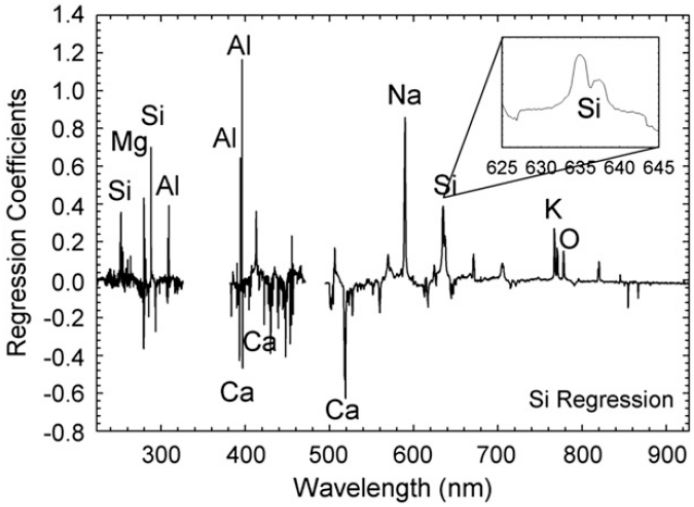

Figure 24. Comparison of PLS regression coefficients to wavelength variables from data set. The behavior of the coefficients clearly identifies which emissions contribute to the variation in the data [8].

then uses a linear combination of values to relate the variation in the spectra with the elemental compositions using a familiar linear equation:

$$Y = b_0 + b_1 X_1 + ... + b_k X_k \tag{13}$$

In Eq. 13, Y refers to the elemental composition variables, and the b terms represent regression coefficients for the corresponding emission wavelength X. This regression model can be used to determine elemental concentrations using spectral data taken from a sample of unknown composition.

A regression model for a data set generated using this technique can be contrasted to one generated using PCR, as both MVA methods could produce models with different levels of accuracy. An example comparison is depicted in Fig. 25. These models were generated in a Mathworks MATLAB tutorial from NIR spectral data of fuels at different octane ratings. These example models compare regression fits relating the

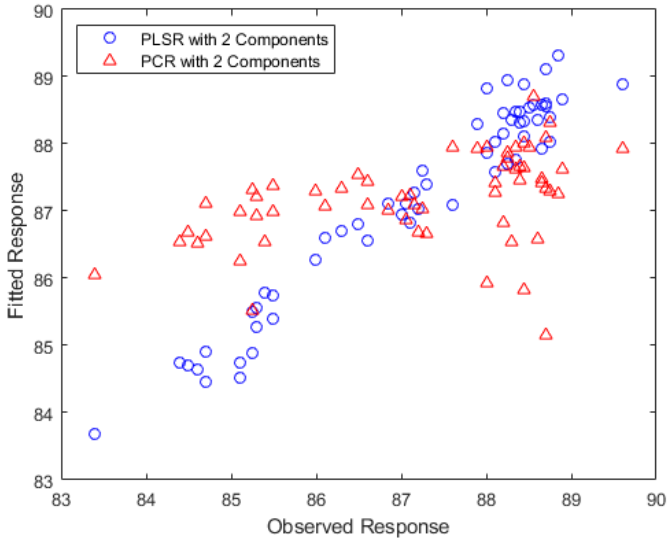

Figure 25. Comparison of regression models generated using PCA and PLSQ [62].

wavelengths of the fuel spectra to the octane rating using 2 components in both models. This plot outlines the main difference between the two regression methods. PCR constructs components to explain variances in the predictor data matrix, while PLSR accounts for the relationship between the predictor data matrix and the responses. As a result, PCR with two components cannot generate an accurate predictive model, since the data the first two components explains most of the variance in the predictor variables, but little of the variance in the responses.

3. Methodology

The Z500 was used in a data collection process similar to the one described in Sect. 2.5.1 to perform quantitative analysis of cerium-gallium compounds. The generated calibration curves were used as confirmation that the Z500-ER is capable of lanthanide analysis. Further multivariate analysis of the spectral data was conducted to refine the calibration models, and limits of detection were calculated. Upon acqui-

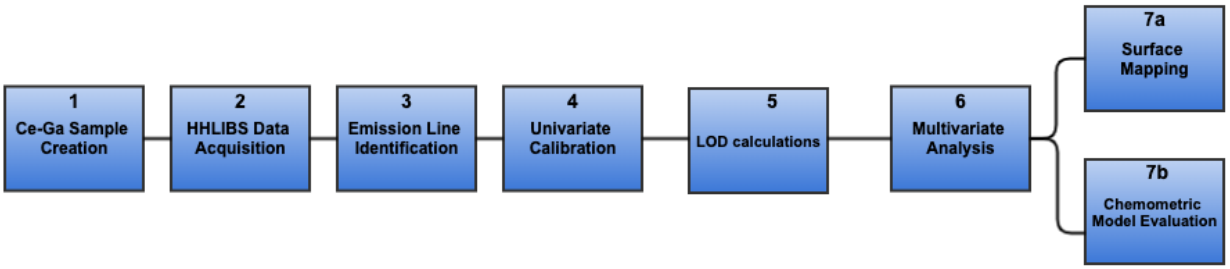

Figure 26. Experimental data collection and analysis flowchart.

sition of the Ce-Ga pieces, the HH-LIBS was used to record spectra from each sample. Next, using information tabulated in literature [33], strong spectral lines to be used in univariate analysis were identified. After line identification, a calibration curve was built to relate the intensity ratios of the selected spectral lines to the concentration of gallium in each alloy sample. Limits of detection for the univariate analysis curves were calculated. Once appropriate emission line ratios were identified, multivariate analysis techniques were implemented to generate higher-fidelity mathematical models relating the behavior of multiple emission lines to the gallium concentration. The multivariate regression model was then used to conduct a detailed surface gallium concentration mapping analysis of a sample to quantify surface anomalies in Ga distribution and evaluate the alloy production process. Lastly, two different multivariate analysis techniques were used to conduct a chemometric calibration of the

sample spectra. These models were quantitatively evaluated and compared against each other to determine the best candidate for use in an analytical program.

3.1 Ce-Ga Alloy Sample Creation

The cerium and gallium alloy samples were made using a Thermo Scientific Thermolyne (model number FD1545M) resistive heating furnace. Cerium metal (99.9% purity) was obtained from Aldrich Chemistry and gallium metal (99.99% purity) was obtained from Alfa Aesar. Preparation of the samples took place in an argon filled glovebox with oxygen content nominally under 200 PPM. Between 10-20 g of cerium metal in chips of approximately 4 g each were weighed using a mass balance (Mettler Toledo PR2003 DeltaRange). Gallium metal was then heated to its liquid state (approximately 60 °C) and measured out using a glass pipette to the desired concentration within the Ce-Ga alloy. Weights of both metals were chosen to create samples between 0 and 3 weight percent gallium; these Ga content levels contain the weight percent range in which Ga can stabilize the delta phase of Pu, as per Fig. 14. The combined Ce-Ga was placed in a magnesium oxide crucible obtained through Fisher Scientific and heated in the furnace to 850°C and held at that temperature for 8 hours. The furnace temperature was then reduced to 480°C and held for 12 hours to anneal the samples. After annealing, the furnace was turned off and allowed to cool via natural convection down to room temperature. The crucible containing the Ce-Ga alloy was removed and cracked with a hammer to release the sample. Samples were then exposed to ambient air and humidity to grow an oxide layer. For the scope of this work, the Ce-Ga samples had been exposed to air for over 3 months.

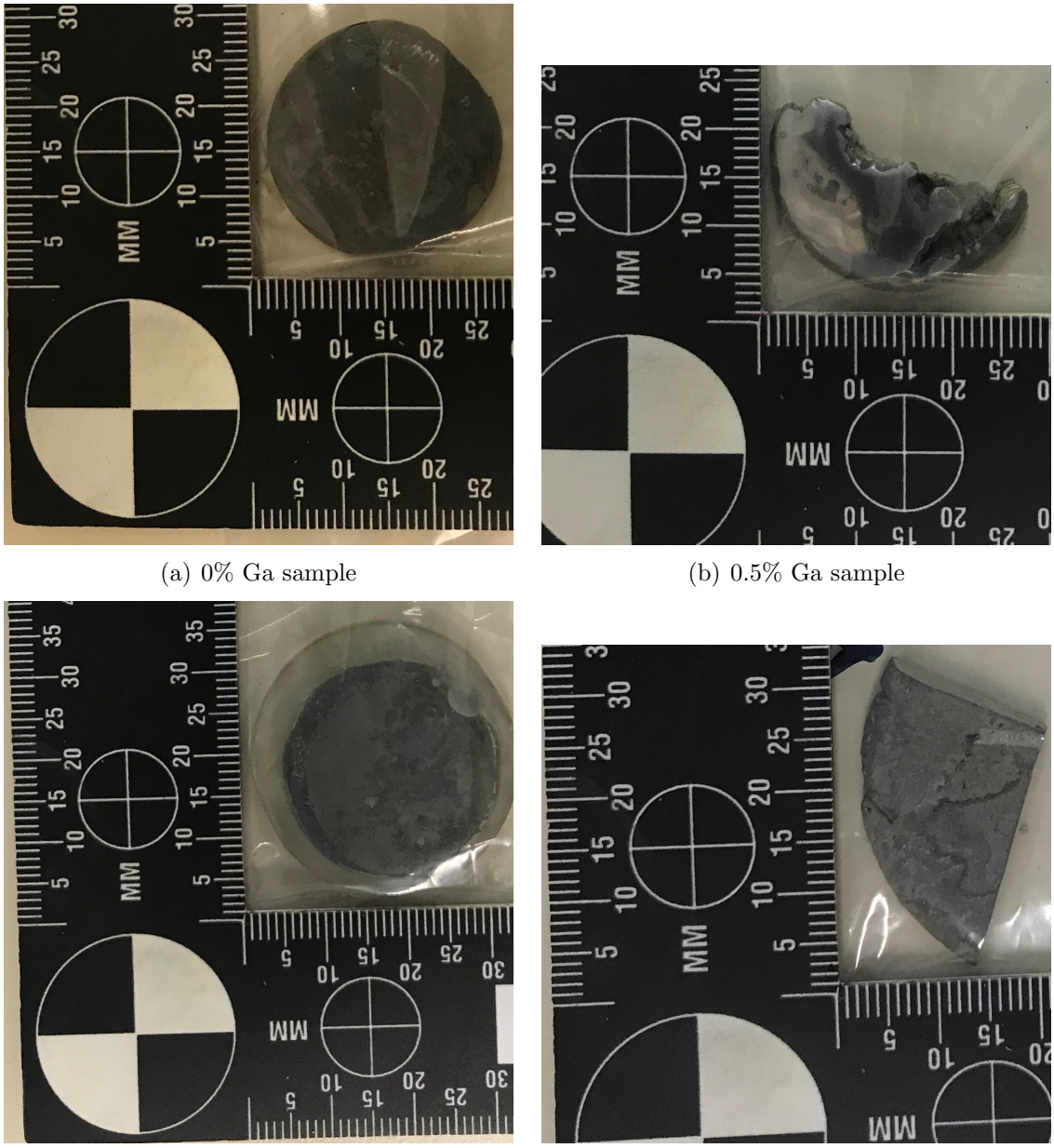

(a) 0% Ga sample

(b) 0.5% Ga sample

(c) 1.0% Ga sample

(d) 3.0% Ga sample

Figure 27. The Cerium-Gallium alloy samples used for the experimental calibration curve measurements. The samples seen in (a), (b), (c), and (d) have Ga weight percent concentrations of 0, 0.5, 1.0, and 3.0 percent, respectively.

3.2 SciAps Z500-ER Handheld Laser Induced Breakdown Spectroscopy Device

3.2.1 Z500-ER Overview

Developed by SciAps in 2014, the Z500-ER was the world's first HH-LIBS analyzer at the time of its commercial release. Its easy to use form, ruggedness, and powerful compact laser made it an ideal device to be used for industrial LIBS analysis. Specification of the devices are listed as follows [16]:

Table 1. Z500 specifications

Laser	Nd:YAG
Wavelength	1064 μm
Pulse Width	1 ns
Pulse Energy	5 mJ
Focal Length	1.5 cm
Spot Size	50 μm
Dimensions	12 x 11 x 5 in
Weight	6.6 lbs
Bandwidth	180-900 nm
Resolution	0.1 nm FWHM

The SciAps Z500-ER used in this work was originally designed for the identification and classification of metal alloys. Its fields of use have expanded into geochemistry and corrosion analysis [17, 63], and the Z500-ER is a promising candidate for field nuclear forensic analysis. A more detailed description of how this system operates for the aforementioned purpose is discussed in Chapter 3.

3.2.2 Elemental Identification Method

The Z500-ER's onboard spectrometer records the radiative emission produced by the microplasma created on the surface of the sample material. The device has an automatic beam rastering function which takes data at different points in the target area, averaging the spectra over multiple spatial points. The device contains many

Figure 28. SciAps Z500-ER handheld LIBS device.

built in programs for elemental identification and alloy analysis, which use pre-built libraries of spectral lines characteristic of various elements.

Upon acquisition of spectral data, the computer examines the experimental spectra and searches the libraries for lines and intensities corresponding to the spectral lines seen in the data. Using the calibration curve technique discussed in 2.3.3, the program generates a list of elements corresponding to the spectral lines from the data, and gives an estimated relative abundance along with a "likelihood" error from which one can derive statistical uncertainty of the measurement [16]. The built-in software also give the user the option to build custom calibration curves for specific materials; this feature can be utilized to expand the capabilities of the device to identify elements whose libraries it does not possess.

3.3 Experimental Measurements and Analysis

3.3.1 Calibration Model Data

The Z500 was used to acquire spectral data on the surface of the Ce-Ga alloy samples ranging from 0 to 3 wt % Ga. Originally, a sample range from 0 to 5 wt % was chosen, however the calibration curves were hindered by self absorption of Ga

emission lines in the 5% spectra, shown in Fig. 29. Since this weight percent is

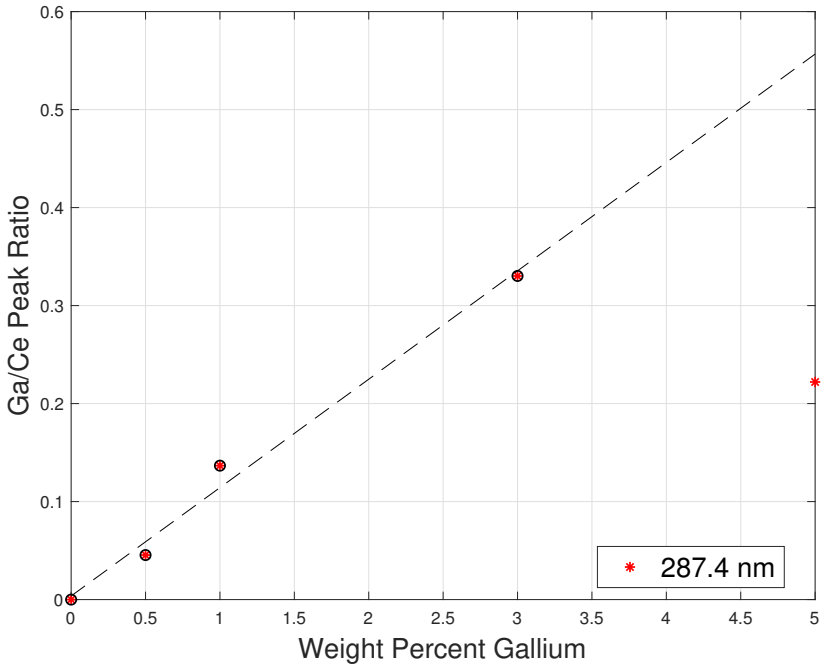

Figure 29. Calibration curve using Ga I 287 nm line with Ga content ranging from 0 to 5 weight percent. Self-absorption is evident; this skews the calibration.

above the delta phase range for Pu, it was not of significant interest to this study, so it was decided that the calibration curves would only include samples up to 3%. The beam rastering function was used to ablate 8 surface locations, with 3 shots per location, and record the average spectra over all locations. This gave a representation of the overall surface concentration. Multiple spectral data sets were taken from each sample. All samples were measured in a glovebox under negative pressure with an argon environment. Data from the spectra was then used to identify strong emission lines of Ce and Ga which could be used to create univariate calibration curves. The complete emission data set was then used to create calibration models built from different multivariate analysis techniques. Limits of detection were calculated for each univariate model to compare their detection capabilities. Statistical parameters such as root mean square error were determined for the different chemometric models

to compare their predictive capabilities and determine which could provide the best solution for an analytical program.

3.3.2 Concentration Mapping

Once the appropriate multivariate calibration curve was generated, the HH-LIBS was mounted to a rig as shown in Fig. 30. Two posts were used to stabilize the base and nose of the device. Cable ties were used to secure the device to prevent sideways movement. Two translation stages were used to create an x-y axis moveable platform upon which the samples were mounted and fixed. The stages were moved to shift

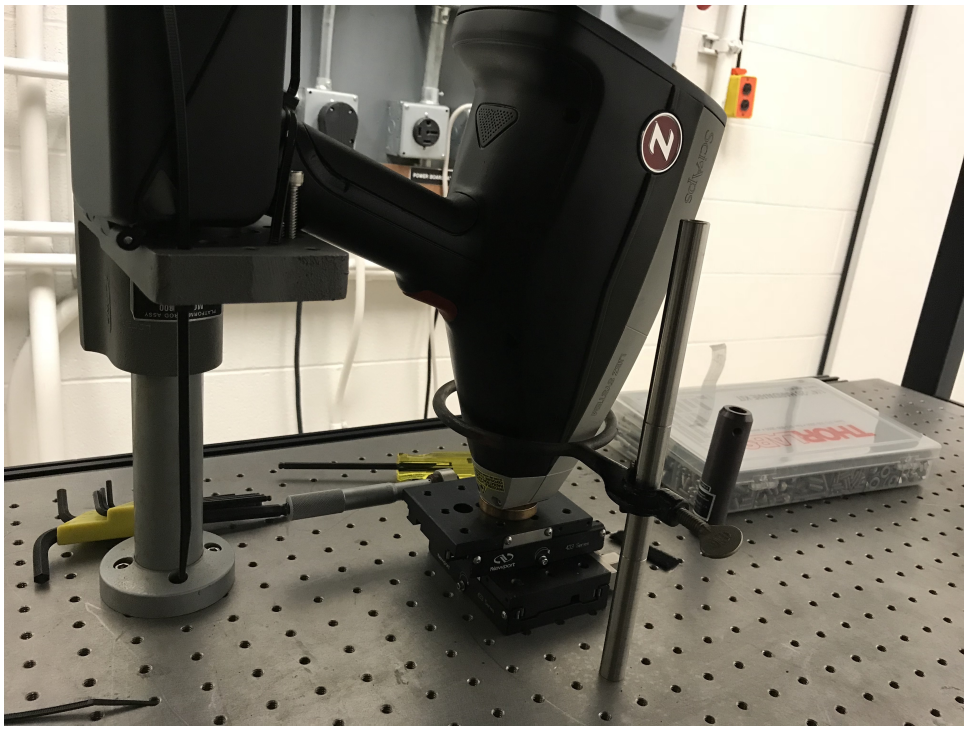

Figure 30. Constructed mount rig used to stabilize HH-LIBS device for mapping measurements.

the sample so that the laser could ablate specific locations across the sample surface. Data was taken in a grid pattern on each sample, keeping the distance between the data points constant at 1 mm. The 3% Ga sample was mapped using this technique, and the MVR model was used to calculate the surface Ga concentration at each point.

4. Results

The previous three chapters provided motivation, background information, and the methodology for the HH-LIBS quantitative analysis experimental study of plutonium surrogate material. This chapter presents the results and is organized as follows. First, the spectrometer settings used to gather spectral data of samples are discussed. Next, the spectral pre-processing method used to remove noise and optimize emission signature peaks is discussed. Then, univariate calibration curves generated from the spectral data are presented. Limits of detection are calculated using the calibration curve parameters. The calibration potential of different line ratios are discussed based on the limits of detection and statistical parameters of the calibration fit lines. Finally, multivariate analysis techniques are applied to the data to generate more complex models relating the emission line intensity to the gallium concentration. Surface concentration mapping results using the multivariate models are discussed, along with the implications and importance of this capability for manufacturing. The accuracy and fidelity each technique is discussed to determine the superior chemometric technique for Ga content determination.

4.1 Spectrometer Settings

The Z500 settings can be modified to fine tune the spectral data acquisition process and maximize the signal. The final settings used for calibration curve data collection are listed in Table 2.

First, a 5 percent Ga content cerium alloy sample was used to collect data to determine gate delay. The optimal gate delay recorded spectral emissions such that signal was maximized and noise was minimized. A gate delay of 450 ns was chosen since this setting gave a strong spectral output signal without the noise seen at earlier

Table 2. Laser and Spectrometer settings used in calibration curve data collection shots.

Settings	Input
Gate Delay	450 ns
Gate Width	250 ns
Locations	8
Shots per location	3
Averaged Spectra	3

gate delay settings; this is reflected in Fig. 31. Some later gate delays, such as the 650 ns signal, showed higher peak intensities, but some of the key Gallium peaks did not appear, as they decayed very quickly after initial plasma formation. The Z500 has

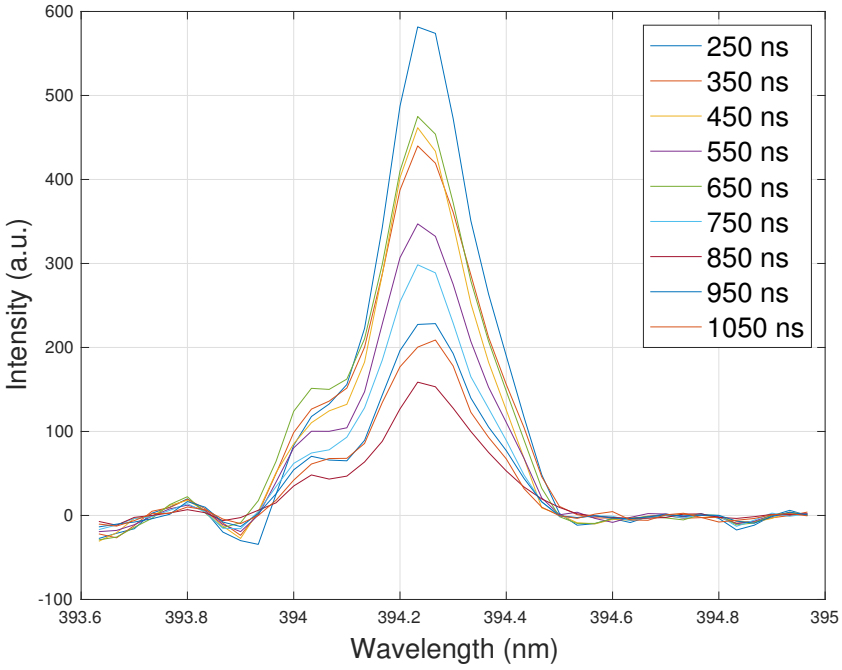

Figure 31. Variation in intensity of Ce 394.4 nm peak with different gate delay settings.

an automatic beam rastering feature which moves the laser focal point during shot collection in order to get a more representative spectra across the target surface. This feature was used to ensure the acquired data was representative of the total sample. To develop a calibration curve, 8 locations were ablated on the sample, with 3 laser

shots per location. These spectra were then averaged by the device. Elemental maps were constructed from a raster pattern consisting of 20 different shots averaged at one surface location.

4.2 Spectral Pre-Processing

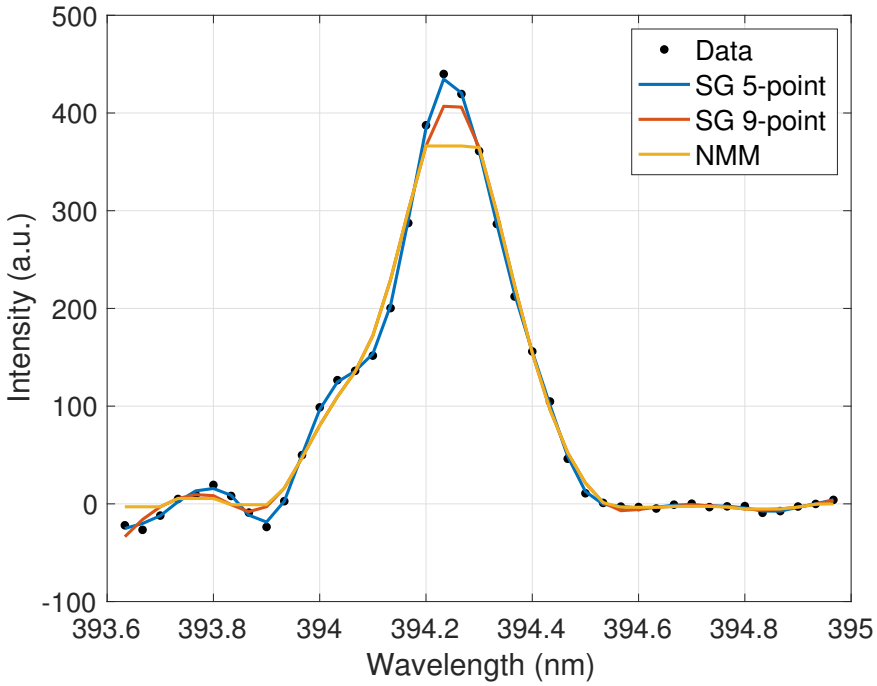

Figure 32. Effects of different individual filters on Ce 394.4 peak.

In order to remove baseline noise and smooth the peak signal, a spectral pre-processing method used by Shattan et. al [17] for analysis of uranium spectral peaks was implemented. This involved a MATLAB routine which conducted 3 processes on the data. First, a signal removal method was employed in order to subtract the baseline from the spectra. This leveled the signal for more accurate analysis. Next, a Savitzky-Golay filter was employed to remove continuum noise from the peak. Finally, a noise median method function was used to further remove noise from the peak wings. The results of varying filter parameters are displayed in Fig. 32.

4.3 Initial Spectral Line Analysis

Spectral measurements of compounds containing the isolated elements of interest were taken in order to get a baseline collection of the various emission lines to compare against the tabulated NIST data. This allowed for initial identification of strong spectral lines which could be used in calibration curves. A gallium oxide (Ga_2O_3)

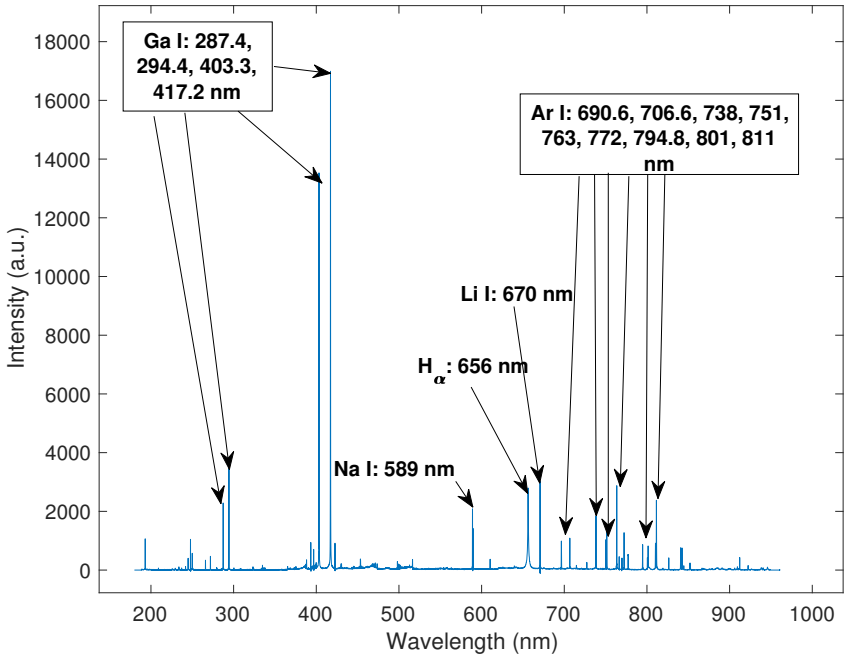

Figure 33. Ga_2O_3 spectra from hand held LIBS device with identfied lines of various elements.

powder sample fixed on tape was used to investigate emission of gallium lines. Fig. 33 displays the emission spectra recorded by the hand held device. 4 main Ga I lines were identified at 287.4, 294.4, 403.3, and 417.2 nm, confirming the data in the NIST database. Additionally, a plethora of argon lines were identified between 690 and 811 nm. These lines resulted from the ionization of the argon fill gas in the glovebox. Additionally, lines from sodium, hydrogen and lithium were identified; these likely came from residual emissions of the ablated tape which was burned through during

a sequence of 75 cleaning shots before recording the ablation of the oxide powder. A cerium oxide (CeO_2) powder sample was prepared for analysis as well. Mutiple

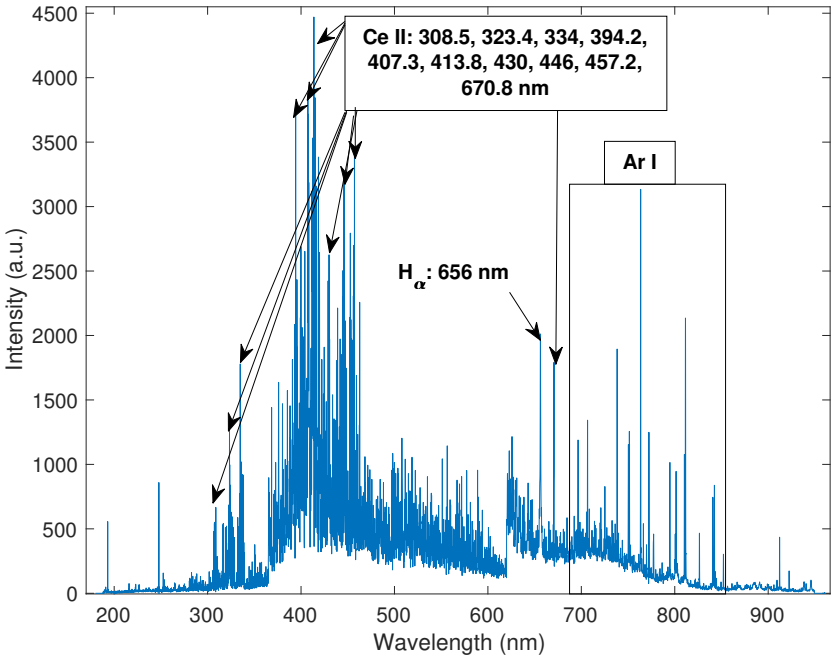

Figure 34. CeO_2 spectra from hand held LIBS device with Ce II lines identified.

tabulated Ce II lines were identified, as seen in Fig. 34. Lines appearing in the lower range of the spectrum were of most interest, since they were less likely to be interfered with by argon emission lines. The Ce II 394.4 nm emission line was determined to be of most interest due to its location in a relatively uncluttered part of the spectrum and its distance from the other Ga I lines. As seen from the figure, the addition of a heavy metal into the sample makes the spectral significantly more complicated. Since heavier elements have more electrons in their electron shells, there are many more electron transitions that can occur, leading to the emission of light at many more wavelengths than is seen with lighter elements.

4.4 Plasma Diagnostic Calculations

The techniques discussed in Sect. 2.2.1 were used to determine electron temperature based on the argon line emissions seen in the recorded spectra, listed in Table 3. The spectra of the recorded argon lines is shown in Fig. 35. The Boltzmann tech-

Table 3. Argon I lines used in Boltzmann temperature calculation [33].

λ (nm)	E_k (cm^{-1})	g_k	A_k (10^6 s^{-1})
738.4	107289	5	0.087
751.5	107054	1	0.043
763.6	106237	5	0.274
772.5	107496	3	0.366
794.8	107131	3	0.117
801.5	105617	5	0.186

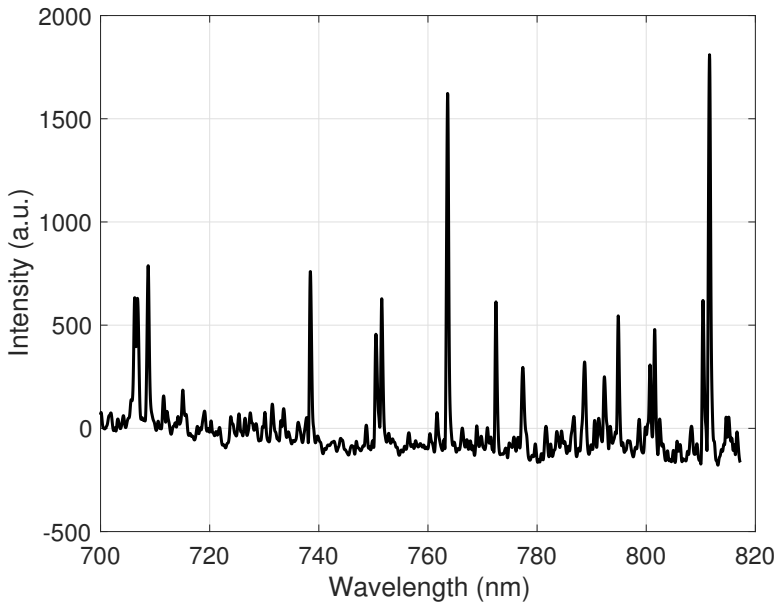

Figure 35. Ar I emission lines used to determine Boltzmann temperature.

nique was used to calculate temperature by averaging the different recorded spectra and using the average intensities of the argon emissions in Eq. 7. This generated a Boltzmann plot, shown in Fig. 36. The inverse slope of the Boltzmann plot gave

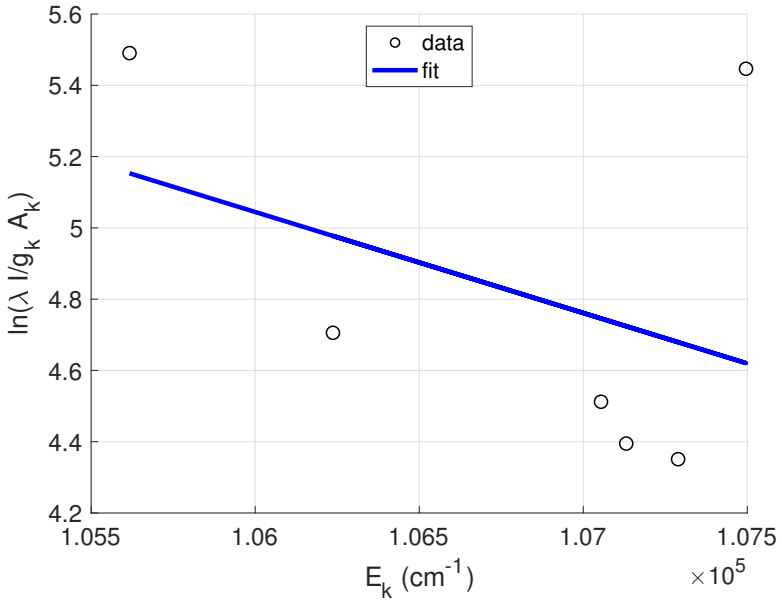

Figure 36. Boltzmann temperature plot points calculated from recorded emissions along with linear fit line.

the electron temperature as 3439 K, or 0.29 eV, giving a characteristic calculation of the temperature of the plasma created by the Z500. However, due to the set integration period of this device, the calculated temperature may be artificially lower than the actual LIBS plasma temperature. The Z500-ER has a set gate width of 1 μs, over which the spectral emission signal is recorded [17]. It has been demonstrated that a LIBS plasma can cool significantly, on the order of 1 eV or greater, over this timescale [29,34]. As a result, the longer integration period of the device caused it to record an averaged signal of a cooling plasma, lowering the calculated electron temperature. Additionally, this temperature could also appear lower due to the recorded signal being a spectral average of the hotter plume center and its colder outer regions. This phenomenon was similarly reflected in the electron density measurements.

The hydrogen alpha peak at 656 nm was seen in the recorded spectra, although significantly diminished compared to many of the other lines. However, the H_α peak was used to conduct electron density measurements by extracting the Stark width via the Voigt deconvolution method discussed in Sect. 2.2.2. The fit is described in

Fig. 37. The Lorentzian width of the peak was determined and used in the following empirical formula developed by Surmick and Parriger to calculate the electron density of the plasma [64].

$$\Delta w_{H_\alpha} = 1.31 \left(\frac{N_e}{10^{17}} \right)^{0.64} \tag{14}$$

The extracted Stark width of 0.3661 nm yielded an electron density of 1.36×10^{16}

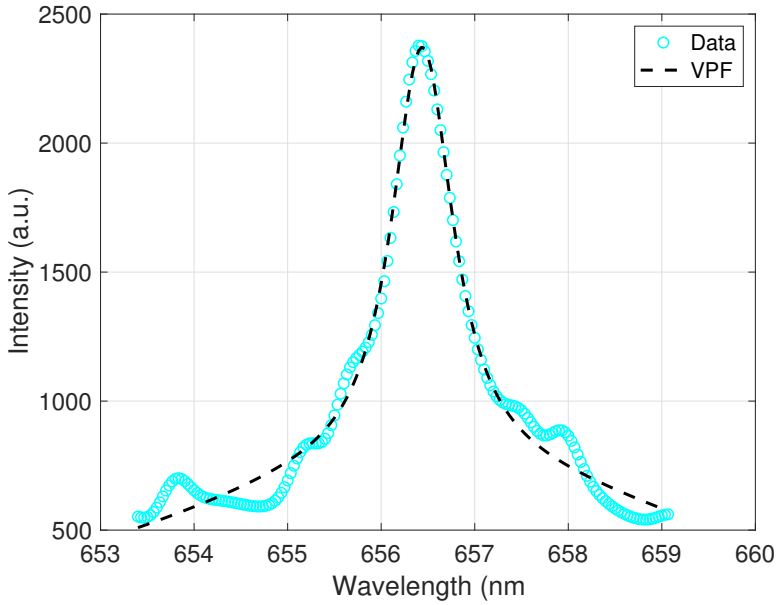

Figure 37. Voigt profile fit to the hydrogen alpha emission at 656 nm.

cm^{-3} using Eq. 14. While LIBS plasmas are typically characterized by electron densities of 10^{16} to 10^{17} cm^{-3}, the longer gate width could have averaged the emission signal while the plasma density was decaying due to cooling and recombination. As a result, this calculated electron density may be lower than the true value.

4.5 Univariate Analysis

Results in this chapter were published in an article written by the author [65]. Rao, A.P.; Cook, M.T.; Hall, H.L.; Shattan, M.B. Quantitative Analysis of Cerium-Gallium Alloys Using a Hand-Held Laser Induced Breakdown Spectroscopy Device. **Atoms** 2019, 7, 84.

4.5.1 Spectral Line Identification

Four emission lines (Ga I 287.4 nm, Ga I 294.4 nm, Ce II 394.4 nm and Ce II 413.8 nm) were identified for use in building calibration curves. These lines appeared across all gallium concentrations tested and were relatively free from other spectral interferences. These lines were extracted from each spectrum and processed according to the routine described in Sect. 4.2. Figs. 38 and 39 display the behavior of the selected gallium lines in the different alloy samples tested. As expected, the intensity of the

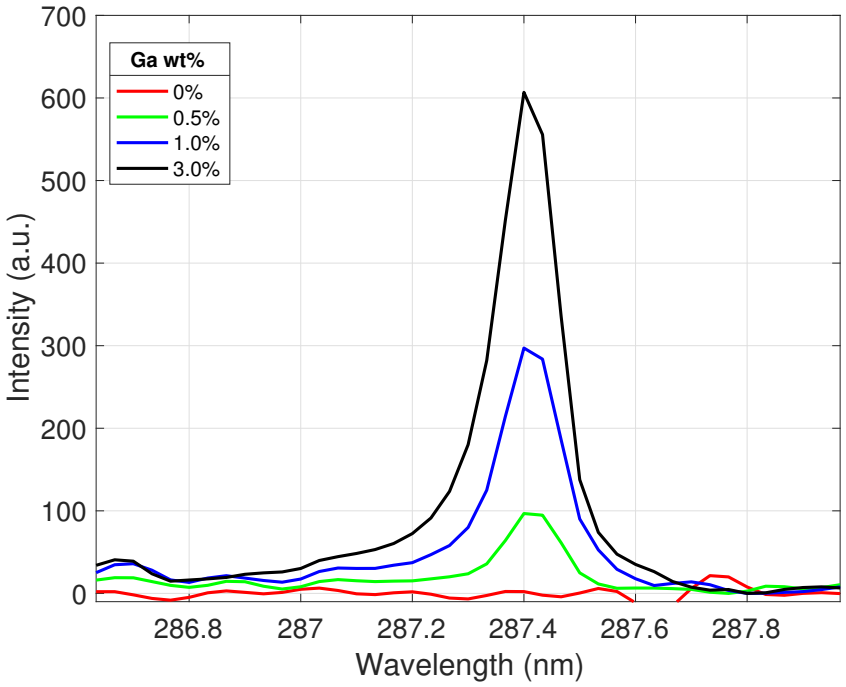

Figure 38. Ga I 287.4 nm peak intensity at different Ga concentrations.

Ga I 287.4 nm emission line increases as the Ga concentration in the sample increases, due to the increasing amount of Ga atoms present to emit the 287.4 nm transition wavelength photon during plasma recombination. This emission line is characterized by a significant emission intensity even at very low gallium concentration levels. The Ga I 294.4 nm emission peak showed similar behavior, with peak intensity increasing as Ga concentration in the alloy increased. It should be noted that the intensity of

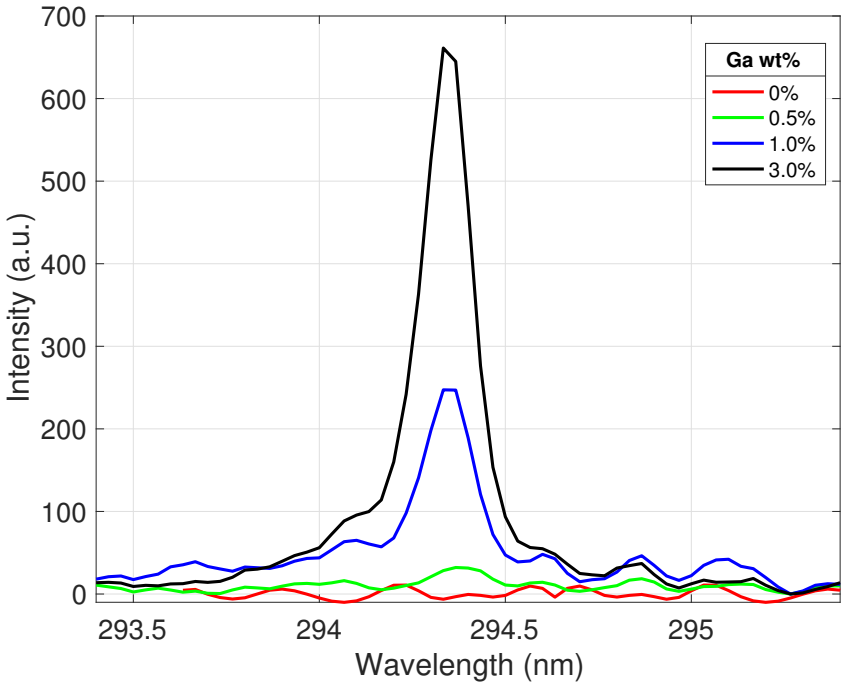

Figure 39. Ga I 294.4 nm peak intensity at different Ga concentrations.

this line in the spectra taken from the 0.5% alloy was significantly lower than the intensity of the 287.4 nm line at the corresponding concentration. The cerium emission peaks at 394.3 and 413.8 nm were similarly analyzed; the results are displayed in Figs. 40 and 41. The cerium emission peaks displayed the expected behavior reflected in the gallium lines; as gallium was added to the alloy, decreasing the concentration of cerium, the cerium emission line intensity decreased. Both cerium emission peaks analyzed showed strong emissions at every concentration level and were free of self-absorption effects or spectral interference from other emission lines. All of the elemental emission lines selected for further analysis showed good responsiveness to gallium concentrations, and their line shapes suggest the plasma is optically thin and free from self-absorption of these emissions. The recorded peak intensities were used to build calibration curves relating peak intensity ratios to sample Ga concentration.

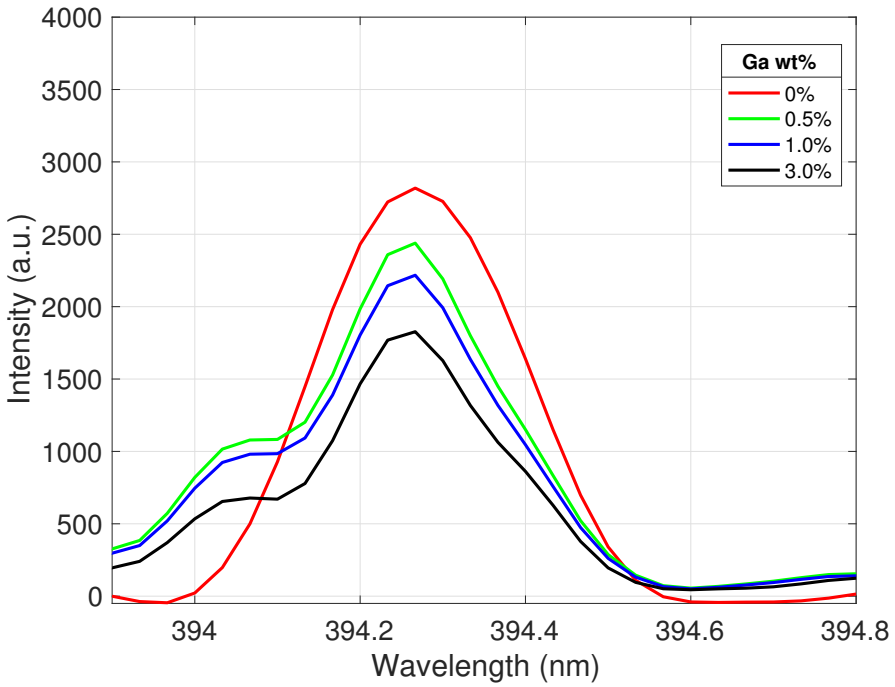

Figure 40. Ce II 394.3 nm peak intensity at different Ga concentrations.

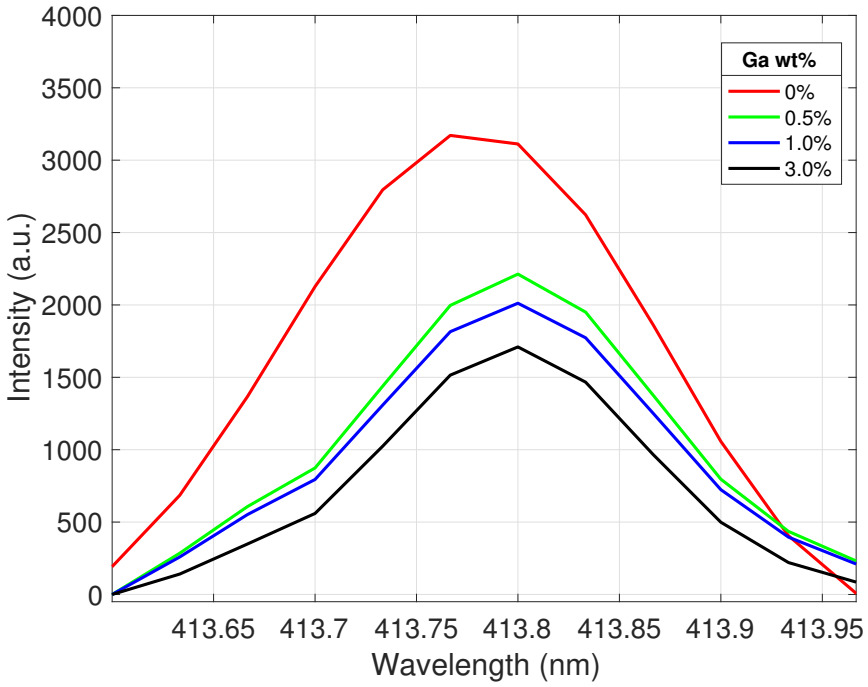

Figure 41. Ce II 413.8 nm peak intensity at different Ga concentrations.

4.5.2 Univariate Calibration Curves

The initial analysis of the Ce-Ga alloy samples examined the emission intensity ratios of the gallium lines to the cerium lines chosen in Sect 4.5.1. Figs. 42 - 45 display the univariate calibration curves using 4 different emission line ratios and display the 95% confidence interval for the regression fit. All ratios from the experimental peak intensity data are represented by the black dots; error was calculated via uncertainty propagation rules using the standard deviation of the selected peak intensities between different shots. The regression fit, displayed as the solid red line, was calculated using a MATLAB function with added weighting factors to each regression point based on the magnitude of the error, thereby including the influence of shot-to-shot peak intensity variation in the fit. This program also returned error bounds for the fit coefficients; these were used to calculate the fit confidence interval represented by the dashed red lines.

Figs. 42 and 43 show calibration curves built using the intensity ratio of the Ga I 287.4 nm emission line to the two Ce II emission lines, while figures 44 and 45 show curves built using the Ga I 294.4 nm emission line. Fit parameters for each curve are listed in Table 4, along with R^2 values and limits of detection (LOD).

Conducting the R^2 analysis for each fit gave an intial metric of how reliable the chosen intensity ratios were for the purpose of Ga concentration calculations. From visual inspection of the calibration curve figures along with a comparison of the R^2 values in Table 4, the Ga I 287.4 nm is clearly superior to the 294.4 nm line for elemental identification purposes. The regression fits made using the 294.4 nm line intensities are extremely poor; the cause stems from the emission line intensities of this wavelength in the 0.5% samples. Comparing the green data line in Figs. 38 and 39, one can see that the 294.4 nm emission is significantly less prominent than that of the 287.4 nm line at a gallium concentration of 0.5%. The large drop in

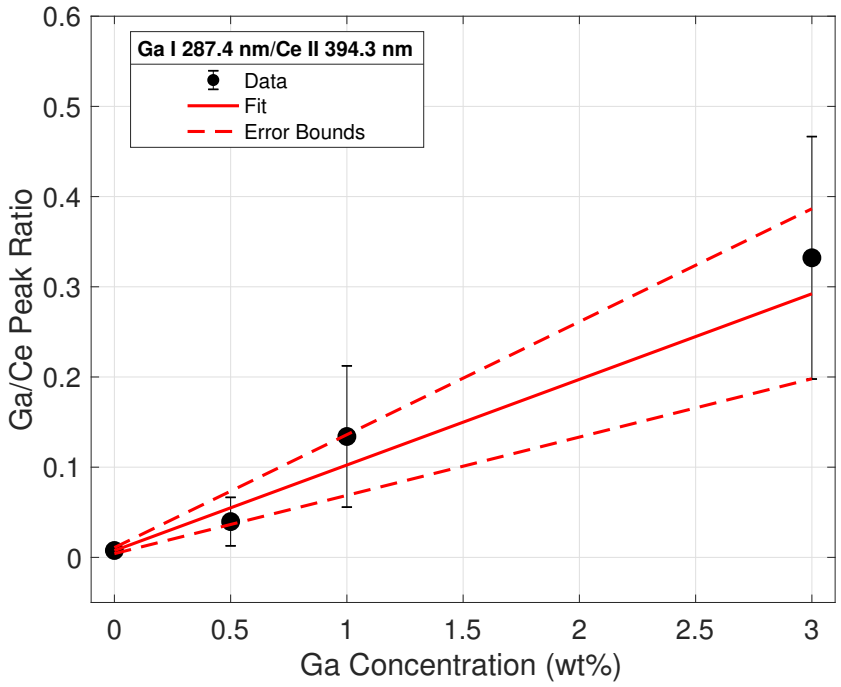

Figure 42. Calibration curve based on intensity ratios of emissions from Ga I 287.4 nm to Ce II 394.3 nm.

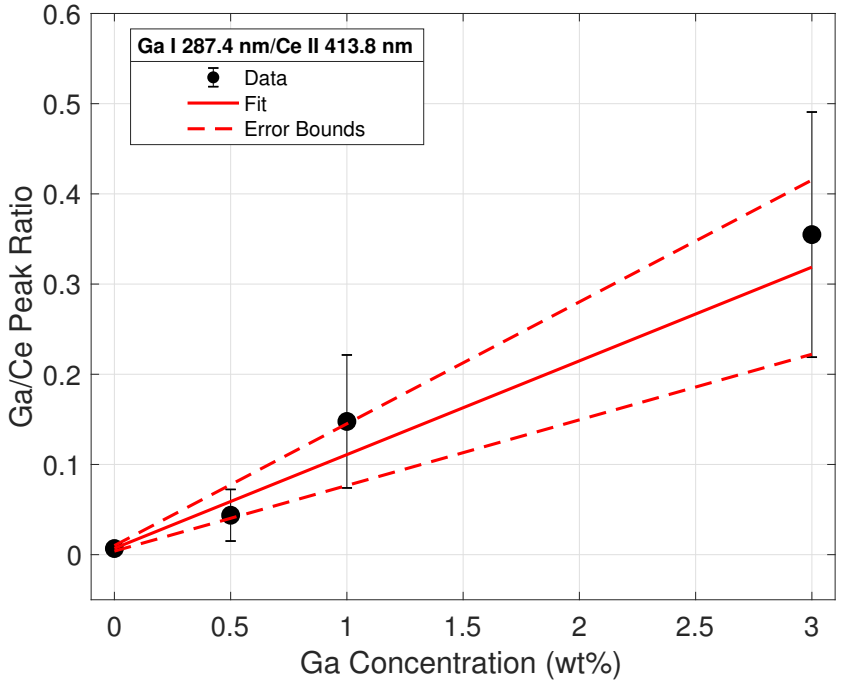

Figure 43. Calibration curve based on intensity ratios of emissions from Ga I 287.4 nm to Ce II 413.8 nm.

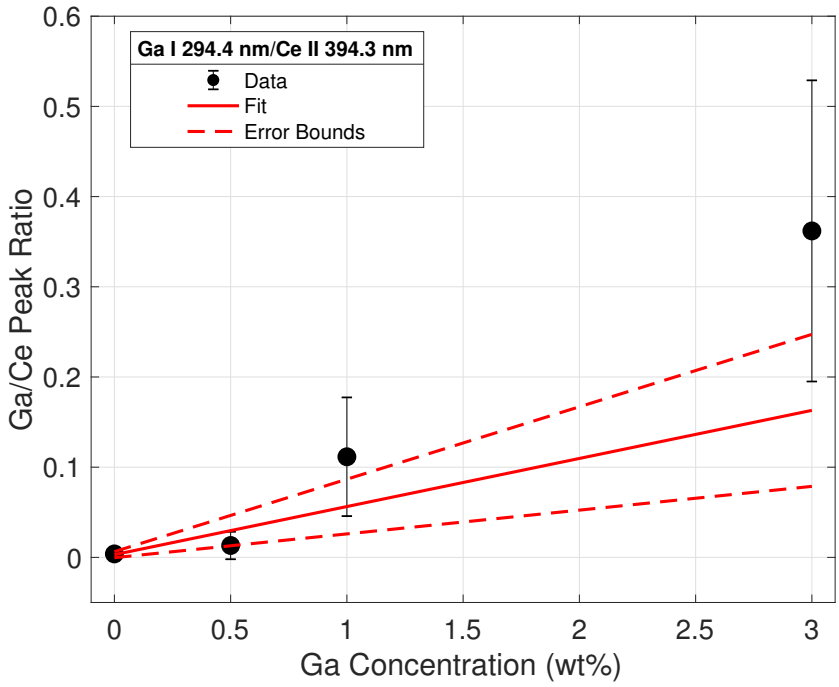

Figure 44. Calibration curve based on intensity ratios of emissions from Ga I 294.4 nm to Ce II 394.3 nm.

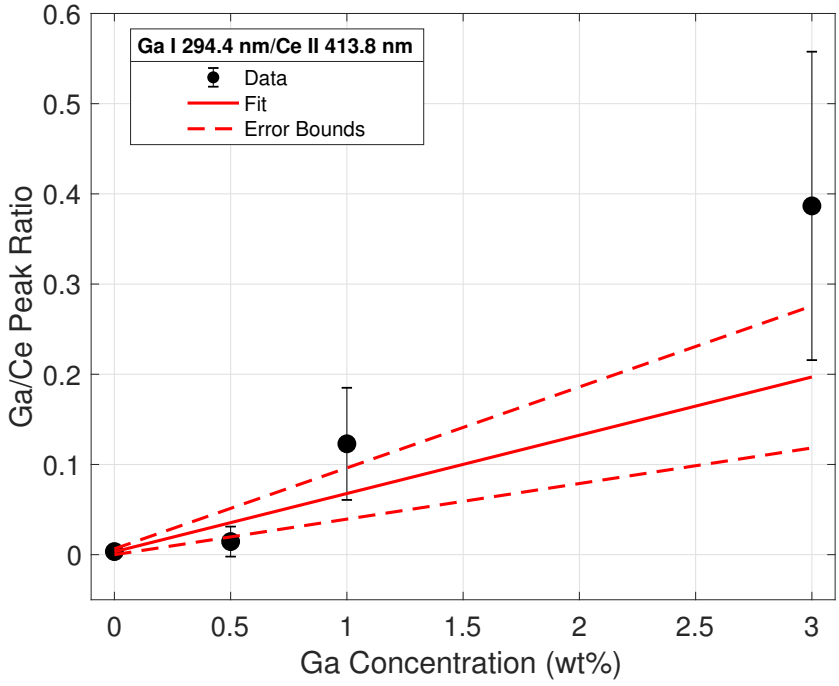

Figure 45. Calibration curve based on intensity ratios of emissions from Ga I 294.4 nm to Ce II 413.8 nm.

intensity of the 294.4 nm peak between the 1.0% (blue line) and 0.5% (green line) samples causes the Ga/Ce peak intensity ratio to drop significantly between these two concentration levels, as reflected in Figs. 44 and 45. The low value of the data point significantly shifts the regression fit lower than would be expected for the given data set, especially when including the effects of error from shot-to-shot signal variation. Therefore, the univariate analysis effectively concludes that the Ga I 287.4 nm emission line is superior for quantitative analysis purposes. Using each of

Table 4. Fitting parameters for calibration curves for equation y = ax + b and Limit of Detection (LOD)

Line Ratio	a	δa	b	δb	R^2	LOD (wt%)
287.4 nm/394.3 nm	0.098	0.0294	0.0072	0.0036	0.9669	0.335
287.4 nm/413.8 nm	0.106	0.0320	0.0066	0.0032	0.9661	0.318
294.4 nm/394.3 nm	0.053	0.0251	0.0029	0.0033	0.4855	3.524
294.4 nm/413.8 nm	0.063	0.0243	0.003	0.0033	0.5637	3.429

the regression lines fitted to the calibration curves, limits of detection (LODs) were calculated for each line intensity ratio. To fully understand the capabilities of each fit, it is critical to quantitatively establish how low of a gallium concentration the different calibration curves could theoretically detection. Having a handheld device capable of resolving Ga concentration differences to the low tenths of a percent would be invaluable to all communities seeking to use the HH-LIBS for quantitative analysis of plutonium surrogates. LODs were calculated using the commonly used expression $3\sigma_d/\mathrm{s}$ [17]. σ_d is referred to as the standard deviation of the blank, and inferred from variations in spectra taken from cerium with no gallium, while s is the slope of each regression fit. The LODs calculated for each ratio from the experimental calibration data further proved the superiority of the Ga I 287.4 nm line for this type of quantitative analysis. An LOD of up to 0.31% was calculated for this line, while the 294.4 nm line curves could not produce an LOD below 3%. This order-of-magnitude difference is likely a result of the low intensity of Ga I 294.4 nm emissions at gallium

concentrations of 0.5%. These initial univariate calibration results indicate promise for the Ga I 287.4 nm line to be capable of resolving small differences in gallium concentration in the sub-1% range. All calculated fit parameters and LODs for each calibration set are tabulated in Table 4.

4.6 Multivariate Analysis

Different multivariate analysis techniques were evaluated with the Ce-Ga alloy data. This section will discuss the calibration model results obtained from multivariate regression, principle components analysis, and partial least-squares techniques.

4.6.1 Multivariate Regression

First, a simple multivariate regression model was created using the built-in MVREGRESS function in MATLAB. By passing in the univariate calibration intensity ratios, error values, and concentration levels to the function, multiple regression fit coefficients were generated to produce a regression model in the form of Eq. 15.

$$y = b_0 + b_1 x_1 + b_2 x_2 \tag{15}$$

Fig. 46 visually represents a basic, 3-D multivariate regression with only 2 predictor variables related to the outcome (concentration). Conceptually, this demonstrates the basic principle behind multivariate analysis. The LOD for this method was calculated using the equation described in Sect. 4.5.2. This 2 factor multivariate model gave an LOD of 0.2435%, a tenth of a percent lower than the best univariate calibration model. This simple multivariate model produced a better LOD than any of the univariate models, highlighting the usefulness of multivariate analysis techniques in elemental identification from LIBS data. The fit parameters to create the model in Fig. 46 are listed in Table 5.

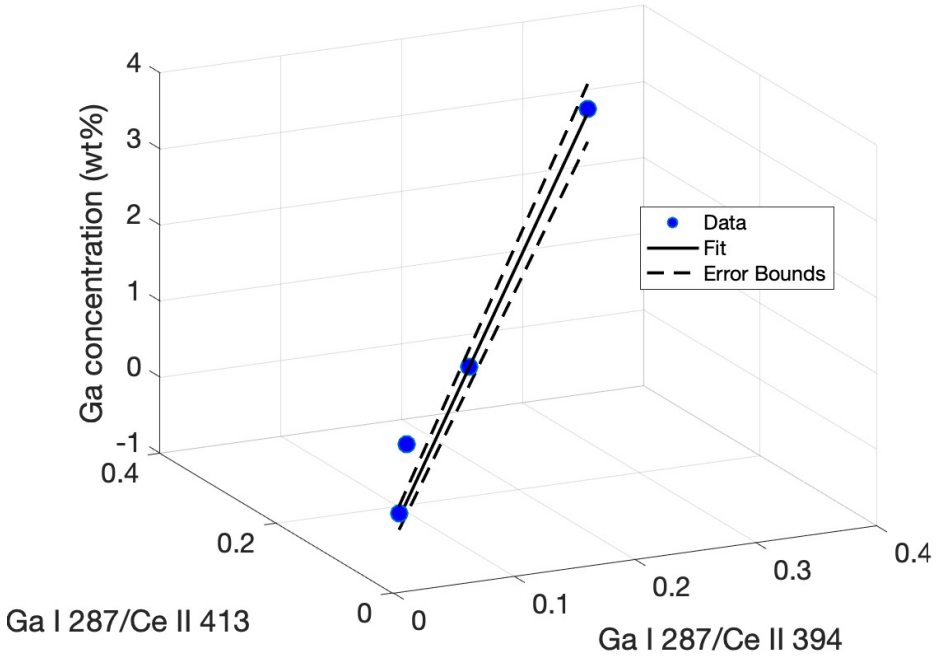

Figure 46. Multivariate regression plot and confidence interval using ratios of Ga I 287.4 nm line to both Ce II emission lines.

4.6.2 Principle Components Analysis (PCA)

As discussed in Sect. 2.6, PCA is a useful multivariate analysis technique for the interpretation of spectroscopic emission data. PCA algorithms can be used to distinguish significantly varying emission lines in a data set, and quantify the interactions and contributions between different emission lines in the sample matrix. This section will provide a detailed overview of the PCA method implemented to cluster the behavior of different cerium and gallium emission lines and represent how the emission intensities of these lines varied with gallium concentration. Sect. 4.5.2 described a univariate calibration based on the behavior of four identified emission lines. To identify additional emission lines of interest, the PCA function in the MATLAB statistics toolbox was applied to 17 different sample spectra recorded with the HH-LIBS. In order to identify significantly varying emission peaks within the differ-

Table 5. Fit parameters for multivariate regression of data points using Ga I 287.4 nm line intensities.

Parameter	Value
b_0	0.006
b_1	2.934
b_2	5.886
δb_0	0.001
δb_1	0.341
δb_2	0.333
R^2	0.994

ent sample datasets, the loadings for each principle component were plotted against emission wavelengths. The loadings of PCs 1-3 of the complete spectrum are shown in Fig. 47. Several additional emission wavelengths corresponding to Ce and Ga

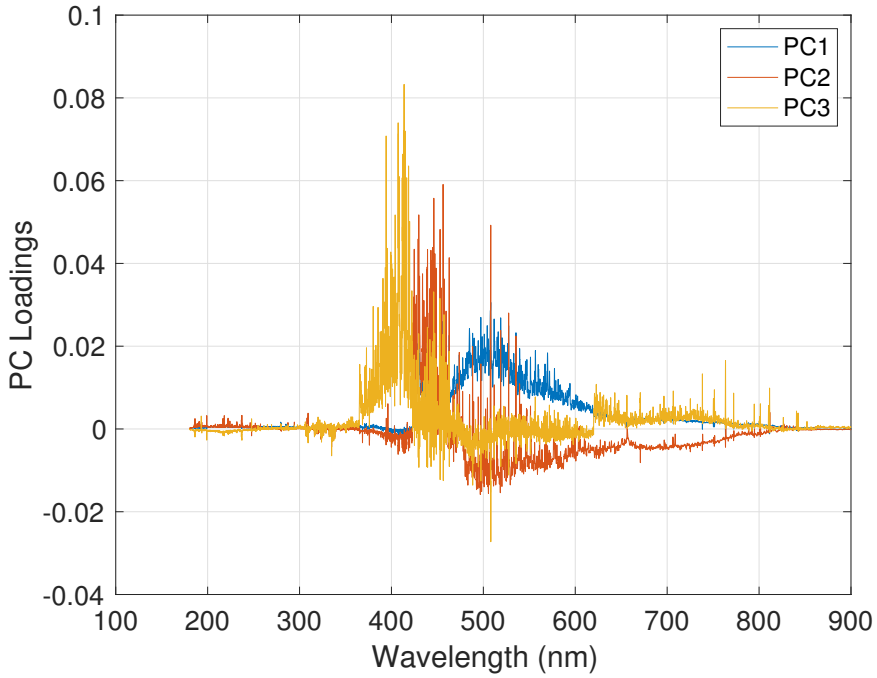

Figure 47. Loadings of all 10 principle components calculated from the Ce-Ga sample data. The peaks which varied the most with Ga concentration show larger loading values.

were identified and used further to refine the PCA calculation, and are listed in Table 6.

Table 6. Emission lines used in PCA algorithm.

Element	λ (nm)	Upper Level
Ga I	287.4	$4s^2 4d$
Ga I	294.4	$4s^2 4d$
Ce II	394.3	$4f5d(^3H^0)6p$
Ga I	403.3	$4s^2 5s$
Ce II	407.4	$4f5d(^3H^0)6p$
Ce II	412.4	$4f5d(^3H^0)6p$
Ce II	413.8	$4f5d(^3H^0)6p$
Ga I	417.2	$4s^2 5s$
Ce II	429.7	$4f^2(^3H_4)6p_{3/2}$
Ce II	446.1	$4f^2(^3H_5)6p_{3/2}$
Ce II	518.8	$4f^2(^3H_6)6p_{1/2}$
Ce II	527.4	$4f^2(^3H_5)6p_{1/2}$
Ce II	535.4	$4f^2(^3H_4)6p_{1/2}$

PCA algorithms output loading values for each principle component; the influence of different spectral lines can be graphically represented by plotting these loadings for different PCs in order to cluster and discriminate the effects of different variables. The influence of individual spectral lines on the discrimination of the selected samples is schematically depicted in loadings plots of the first three PCs. Fig. 48 compares the loadings of the first two PCs of the data. Comparatively plotting PC loadings yields clusters of the data; in this case, each cluster grouped data based on constituent element. The cerium loadings are split into two different clusters; the first cluster, corresponding to the last 5 emission lines in Table 6, appear to be the most significant discriminators in the data set. To investigate the clustering split of the cerium emissions, the 3rd PC was analyzed. As seen in Fig. 48, the 3rd PC further discriminates the cerium emissions into three separate clusters. Upon comparison to the data listed in Table 6, it appears that a possible explanation of this clustering trend stems from atomic deexcitations. Each cerium cluster contains loadings corresponding to emission line variables with similar atomic orbital designations. The red

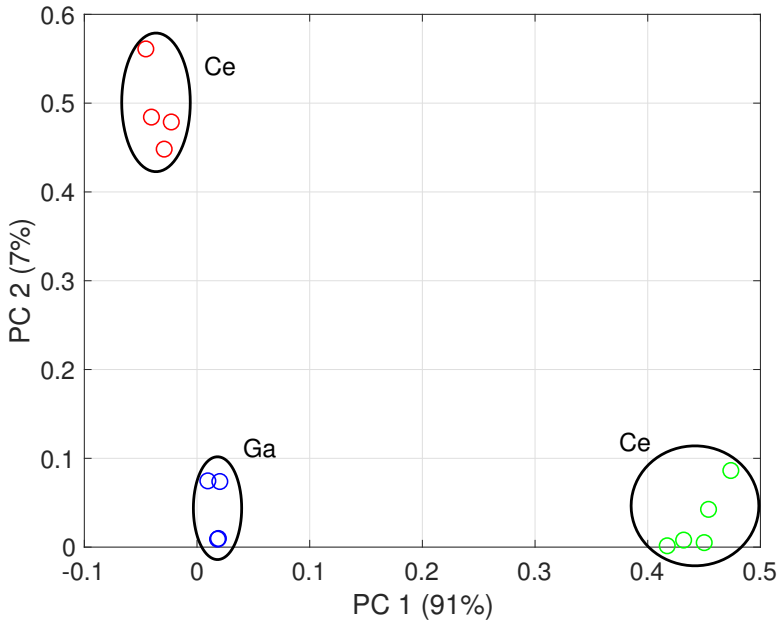

Figure 48. Principle component loadings comparing coefficients of components 1 and 2. The PCA algorithm clusters similar loadings of like elements.

cluster corresponds to Ce emission lines whose orbital transitions start at an upper level of 4f5d(^{3}H^0)6p. The two data points in the upper right Ce cluster both have $6p_{3/2}$ terms, while the three clustered in the bottom right of Fig. 49 correspond to transitions starting at $6p_{1/2}$ upper levels. This analysis of the first three PCs of the data yields several important conclusions. First, the higher wavelength Ce emission lines are the most important for analysis of the sample set, and contribute most to the sample correlations. Second, the PCA algorithm is capable of resolving the complex cerium-gallium spectra into a few key variables, and clustering those variables in ranges based on constituent elements. Lastly, the first three principle components are capable of grouping and resolving differences between emissions down to the atomic level, despite the fact that the PCA algorithm is "physics-blind", as it does not factor sample composition or atomic transition parameters into the calculation. Since heavier metals tend to produce a significant amount of different atomic transitions when elevated to an excited state, this clustering tool can be used to identify specific

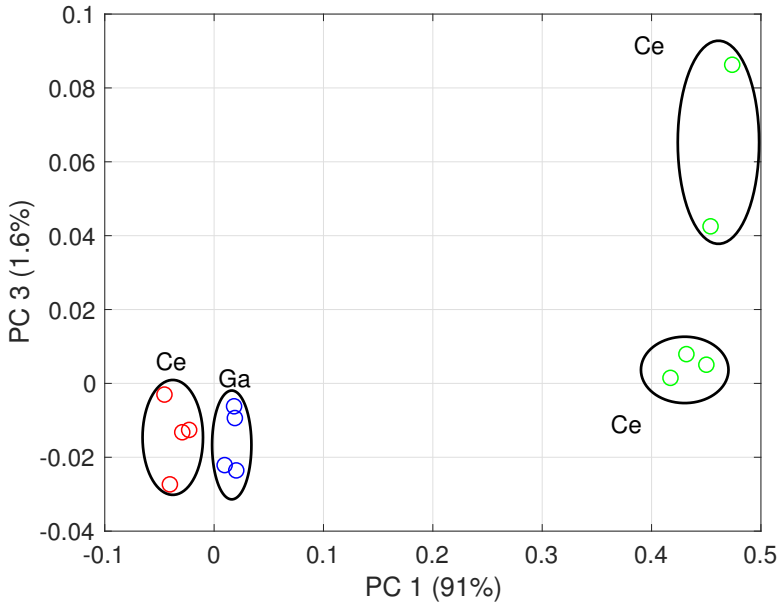

Figure 49. Principle component loadings comparing coefficients of components 1 and 3.

upper energy levels whose transitions are most important and contribute to the most variance in the data set.

While loadings are useful for discriminating sample elements and representing variable correlation, PCA scores plots can represent patterns and resolve differences in the sample distribution. Fig. 50 represents the first three PC scores; the data points are identified by the Ga concentration of the sample from which they were taken. This 3D plot of the scores can be rotated to observe different patterns and features that are similar in the sample set. Fig. 51 relates the scores of the first two PCs. There is a clear clustering of the 0% and 0.5% samples, while the 1% and 3% samples are grouped close to each other, indicating that the first two PCs cannot produce good separation between the 1 and 3 wt. % samples. There is a stray outlier data point corresponding to one of the pure cerium samples, but the overall similarities and patterns in the samples are visually represented. Rotating Fig. 50 allows for further comparison of scores of different components to observe different sample clustering patterns. Fig. 52 demonstrates a better grouping of the pure Ce

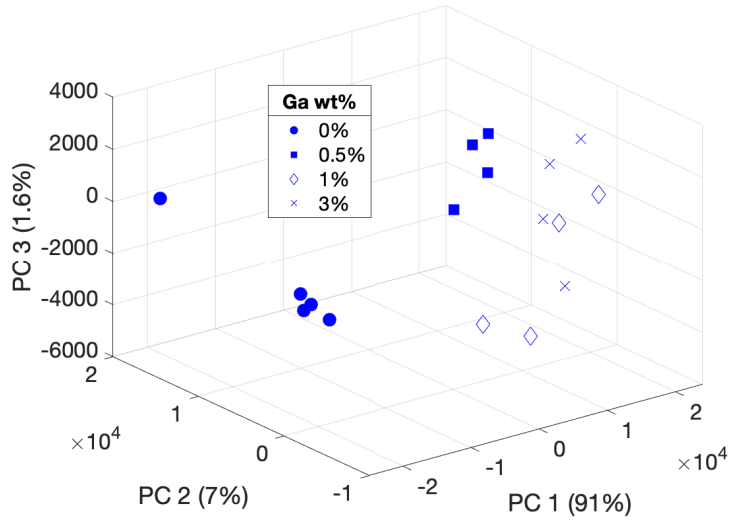

Figure 50. Principle component scores comparison between PC 1, PC2 and PC 3. Clustering based on Ga concentration is evident.

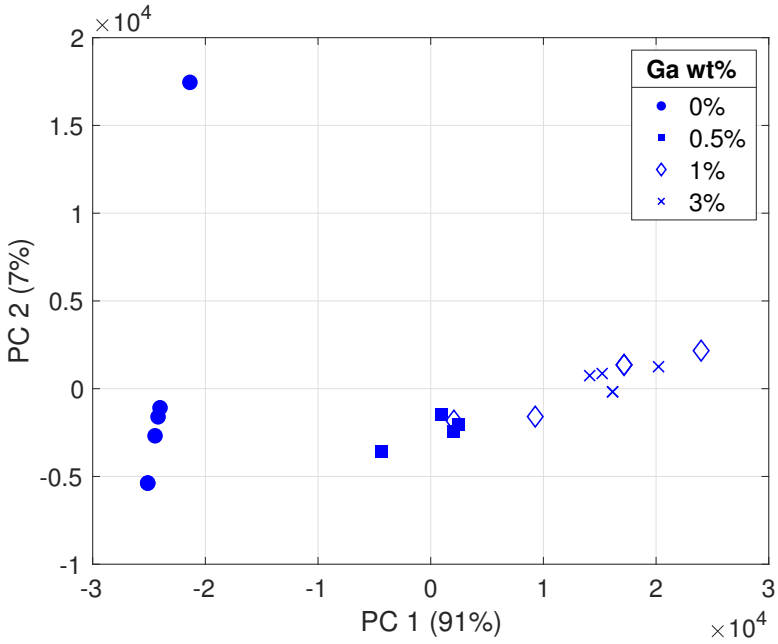

Figure 51. Principle component scores comparison between PC 1 and PC 2. Clustering based on Ga concentration is evident.

samples, and resolves differences between the 1 and 3 percent Ga samples with the exception of one overlapping sample point. While the patterns are more resolved, there is still minimal separation between the 1 and 3 wt% samples when compared to the 0 and 0.5 wt. % points in the same figure.

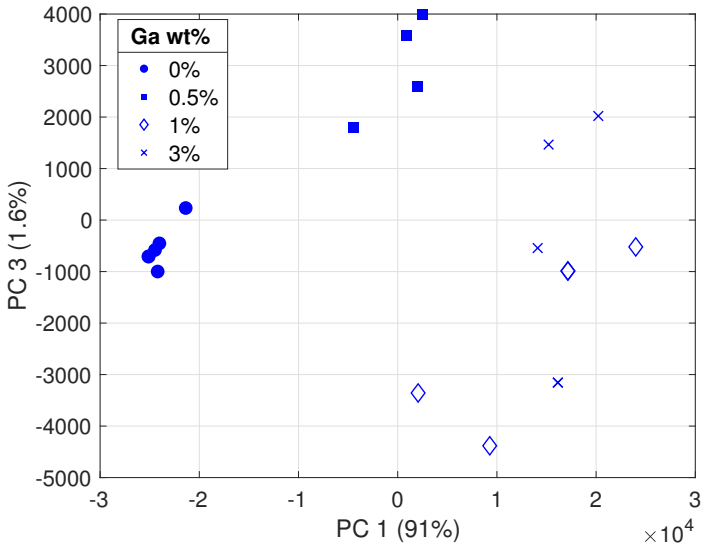

Figure 52. Principle component scores comparison between PC 1 and PC 3. Clustering based on Ga concentration is evident.

Better separation of the higher Ga content samples was achieved by comparing the fourth PC to the first two PCs plotted in earlier figures. Fig. 53 compares scores of PC 4 to PC 1, indicating a much clearer separation of the 1 and 3 wt. % samples, again with the exception of one overlapping point. This indicates that while the first 2 PCs explain an overwhelming percentage of the variance of the original data set, the 4th PC contains the data which resolves the differences between the spectra of the 1 and 3 wt. % samples. The 4th PC only explains a tenth of a percent of the total system variance, indicating that there are relatively few differences in the spectra when Ga content is increased from 1 to 3 wt. %. However, for the purposes of creating a discriminative Ga content determination algorithm, this result indicates that a larger number of principle components may be needed to distinguish between

the spectra of higher Ga content alloy samples.

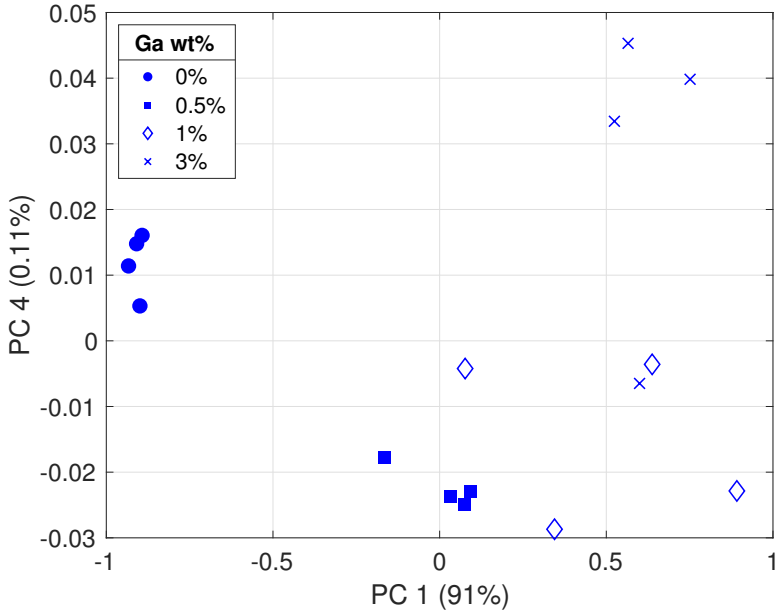

Figure 53. Principle component scores comparison between PC 4 and PC 1. Separation of the 1 and 3 percent samples is noticeable along with more distinct grouping of the pure Ce and 0.5 percent Ga samples.

Analysis of the PC scores can yield important information about the features and relationships between sample data points. The behavior of samples in different dimensions of the scores plot can be used to construct a predictive model, in which the position of different PC scores in various planes of the 3D component space can help determine the Ga concentration of an unknown sample by comparing it to the tabulated PC scores. This initial analysis of the spectral data using PCA was extended to build a predictive regression model of the data set. The results are compared to a predictive model generated using partial least-squares regression to evaluate the capabilities of the different multivariate techniques.

4.6.3 PLSR vs. PCR

Predictive models built using PLS and PCA have varying degrees of accuracy due to differences in the numerical calculations both algorithms perform on a given data

set. Finding the best model to use in order to maximize accuracy of elemental content determination and minimize computational time required by the HH-LIBS is a critical portion of this study. While PLSR and PCR both represent dimensional reduction techniques capable of explaining a data set in terms of simplified latent variables, PLSR yields covariance coefficients which explain variance in both the predictor and outcome data. The percent of variance explained in the Ga content measurements (outcome) of the sample spectra in each decomposed component is plotted in Fig. 54. The figure indicates that 5 PLS components are necessary to explain more than

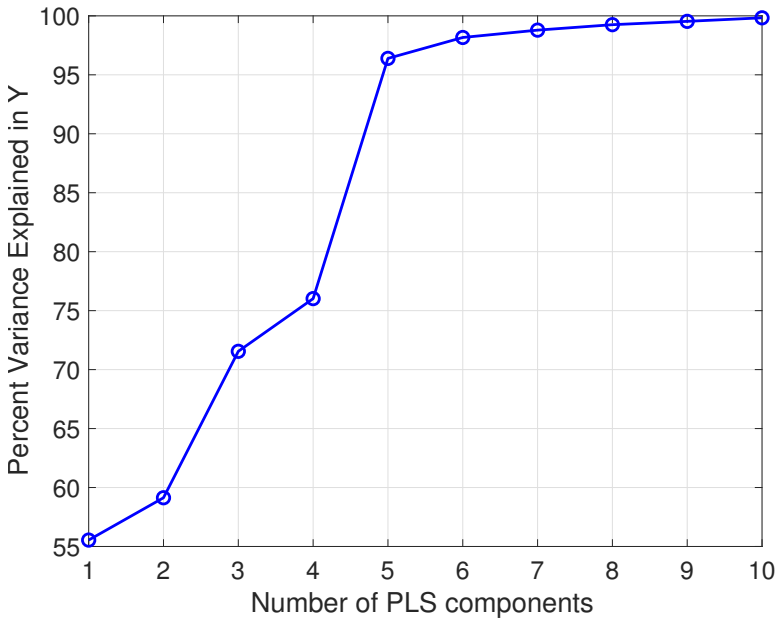

Figure 54. Partial least-squares regression component variance plot. 95% of variance in the data is explained with 5 components.

95 percent of the variance in the Ga concentrations across the sample set. For the purposes of creating an analysis routine to be run by the Z500's onboard computer, using a PLS or PC regression with less components would be less computationally intensive, leading to quicker analysis times. Initially, both PLSR and PCR algorithms were run with the spectral data set, using a maximum of 5 components for each technique. Initial insights can be gleaned from plotting the scores of the first two principle components of each technique against the Ga concentration in the sample

set.

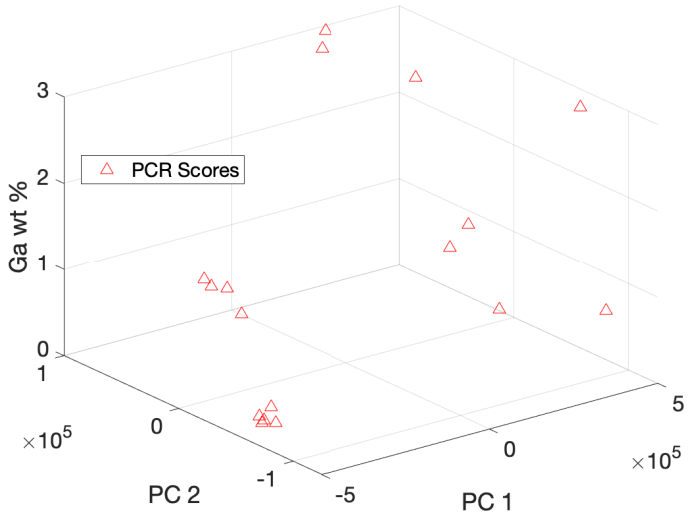

Figure 55. Comparative plot of scores of first three PCs from PCR model.

As demonstrated in Sect. 4.6.2, PC scores can be used to cluster sample sets based on similarities in the data. In this case, the scores used to produce the PCR model group each sample based on Ga content, as seen in Fig. 55. Here each sample point is clearly clustered with its corresponding Ga concentration. The same behavior is observed in the score variables generated from PLSR, as demonstrated in Fig. 57. While clustering the sample set is useful in qualitatively analyzing similarities in the data set, regression models must be statistically analyzed to determine the quality of the calibration. The PLSR and PCR calibration models are plotted in Fig. 59.

The calibration models are compared by plotting the fitted regression response against the observed response from the data set. Upon initial inspection, the figure clearly reflects that the PCR response is less linear than the PLSR model response. Qualitatively, it can be deduced from this figure that the PLSR model provides better predictive capabilities for purposes of calibration and impurity detection. These models can be quantitatively compared by examining the differences in their R^2 and root mean square error of cross validation (RMSECV) values, which are listen in Table 7.

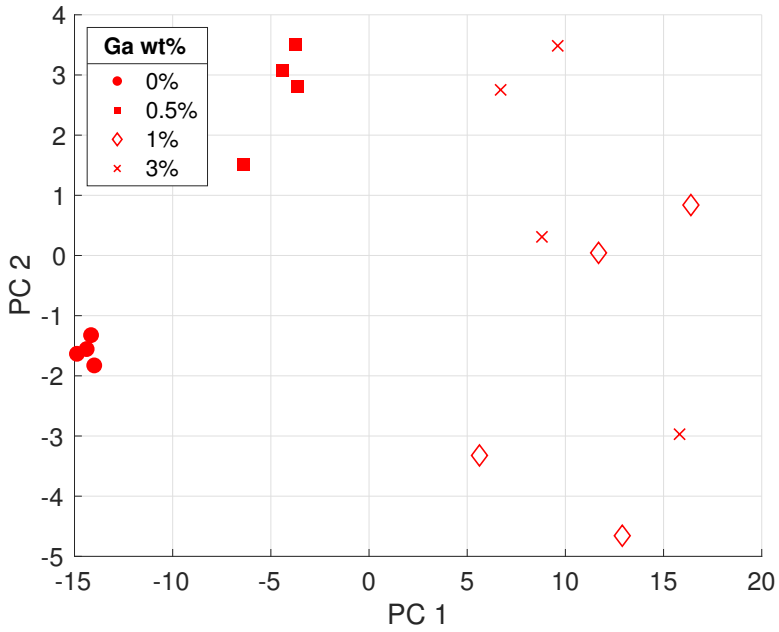

Figure 56. Comparative plot of scores PC 2 vs PC 1 showing sample classification based on Ga content.

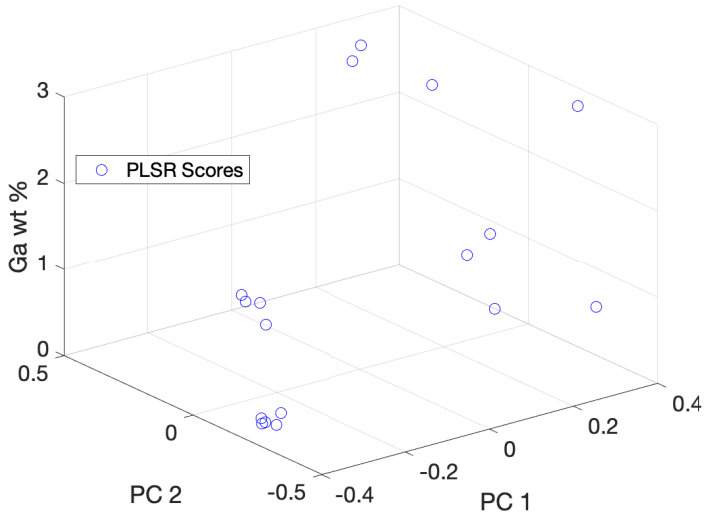

Figure 57. Comparative plot of scores of first three LVs from PLSR model.

Table 7. RMSECV and R^2 values of PCR and PLSR models

	PCR	PLSR
RMSECV	0.716	0.216
R^2	0.603	0.964

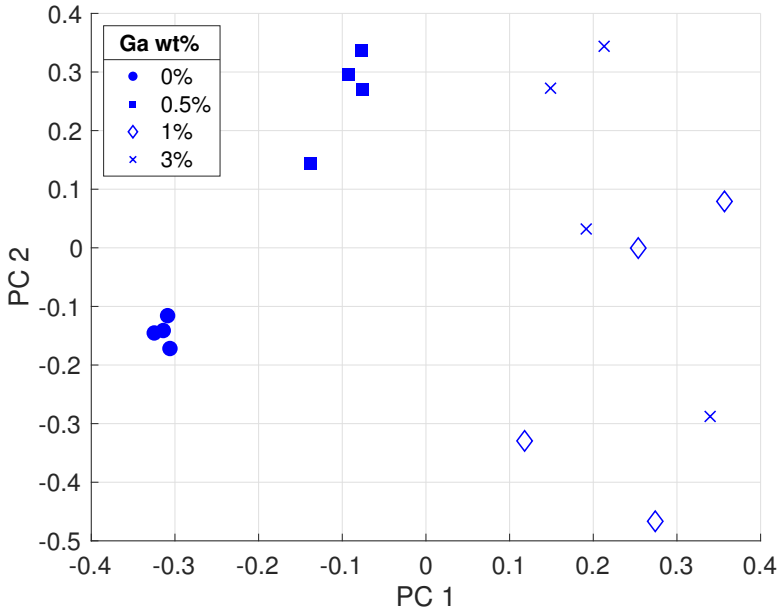

Figure 58. Comparative plot of scores of LV 2 vs LV 1, showing similar sample classification patterns as PCA.

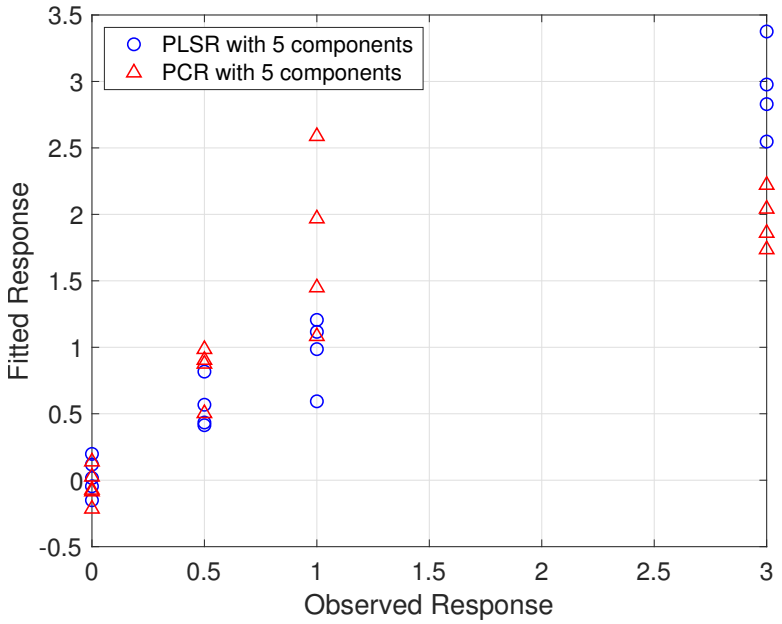

Figure 59. Comparison of measured and predicted Ga concentration using PCR and PLSR models.

The PLSR model has a much higher R^2 value than the PCR model, indicating a higher linearity and fidelity in the regression. Additionally, the RMSECV value of the PLSR model is significantly lower than that of the PCR model, suggesting a more accurate calibration due to the fact that the error between the fitted and observed responses is much lower in PLSR. As reflected in Fig. 60, PCA explains more

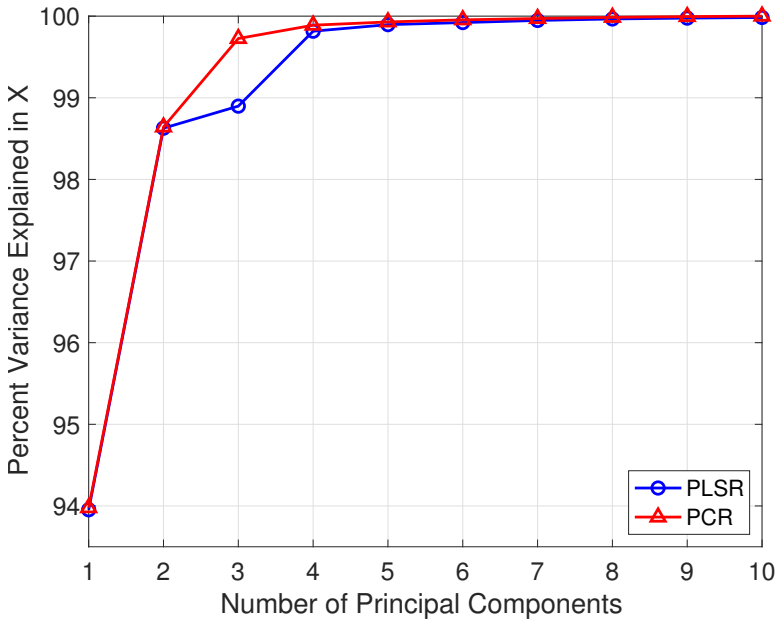

Figure 60. Comparison of variance in X explained by PCR and PLSR.

variance in the predictor with less components than PLS does. However, since the PLS regression factors in the variance of the outcome variables, it produces a better fit than PCR with the same amount of components; these same results are quantitatively reflected in Table 7. In conclusion, the multivariate analysis investigation of the Ce alloy spectral data proved that PLSR is the superior analysis technique for the purposes outlined by this study. Due to its ability to accurately fit a sample data set, PLSR provides the best possibility for building a computationally effective predictive model which can be programmed into the Z500's onboard computer. This conclusion is verified by examining the full component fit model, shown in Fig. 62 and quantitatively described in Table 8.

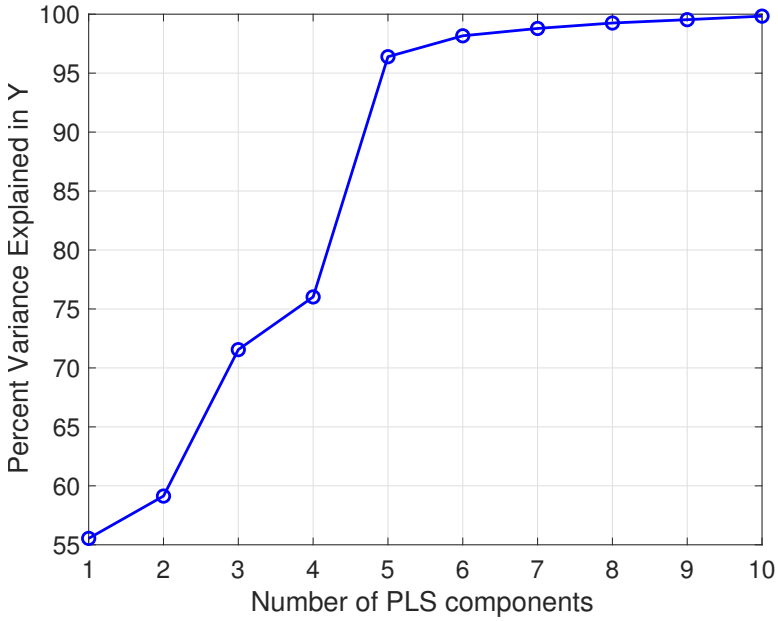

Figure 61. Percent of total sample set variance in the outcome explain by each PLS component.

Table 8. RMSECV and R^2 values of full component PCR and PLSR models

	PCR	**PLSR**
RMSECV	0.140	0.046
R^2	0.985	0.998

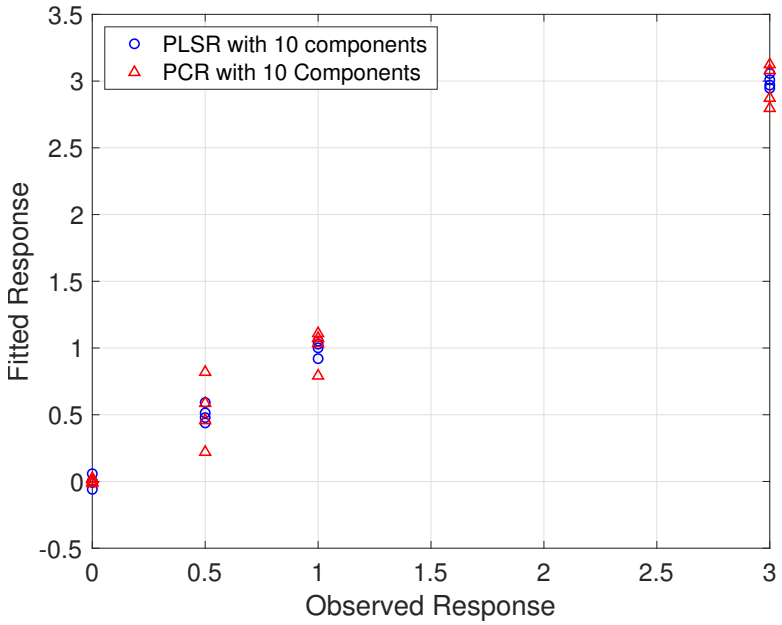

Figure 62. Comparison of measured and predicted Ga concentration using 10 components PCR and PLSR models.

While the regression fits appear to both be extremely linear and show the same agreement between the experimental and calibrated Ga content, the R^2 and RMSECV values still indicate that PLSR provides the superior multivariate model even with all ten components being used.

4.7 Surface Gallium Concentration Mapping Results

The HH-LIBS was mounted above a 2-dimensional translation stage and the alloy samples were fixed to the stage. A series of shots were recorded at 1 mm intervals across the surface of each sample. The multivariate regression model developed in Sect. 4.6.1 was implemented on the spectra recorded at each location to calculate Ga concentration at each ablation point. The surface Ga concentration distribution of the 3% sample is depicted in Fig. 63. This map can be analyzed to evaluate the sample production process and examine the uniformity of the temperature in the crucible during the annealing cycle used to diffuse the gallium through the molten cerium

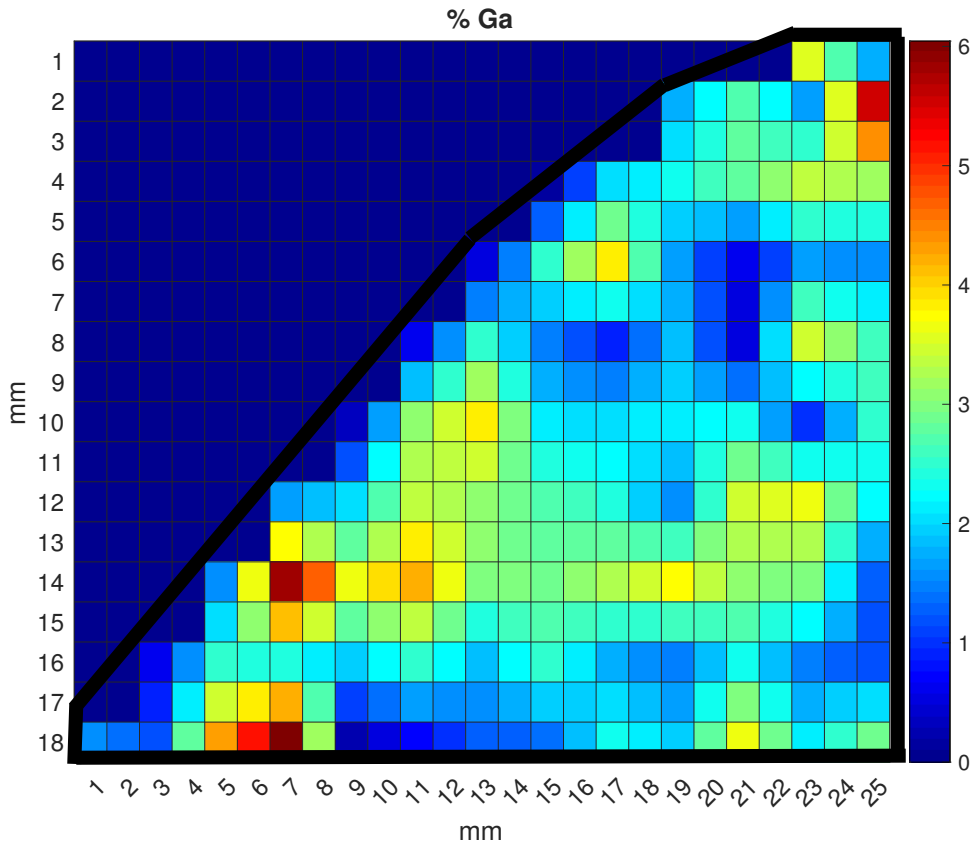

Figure 63. Map of Ga concentration of a 3 % Ce-Ga alloy sample across the surface of the sample.

metal. Non-uniform heating of the inner crucible surface can cause an improper diffusion of gallium through the crystal lattice of the bulk metal. Additionally, since the surface exposed to air is not heated at the same rate as the surfaces contacting the crucible, gallium atoms tend to diffuse inwards towards hotter areas in the metal. This causes a lower gallium concentration on the surface, with gallium tending to crystallize instead of dispersing evenly through the cerium. This explains the regions in Fig. 63 of below 1% Ga concentration with a few points having a 5 or 6% concentration.

This result yields several important conclusions. Firstly, it indicates that the hand-held device can be used to conduct a rapid, detailed surface analysis to evaluate production quality of the alloy. Secondly, by mapping the impurity concentrations across the surface of a metal and examining the distribution, the manufacturer can

modify the alloy creation process (i.e. change the melting, forming, annealing stages) in order to create a better alloy with a more even distribution of the dopant metal. Lastly, this result indicates that this same method of analysis can be applied to Pu-Ga alloys to ensure their quality and uniformity during production. As seen earlier in Fig. 14, a very particular weight percent of Ga produces δ-Pu at room temperature. Anything below this range leads to the formation of α-Pu crystals in the alloys, while excess Ga can cause the formation of the ξ" phase. Since the different allotropes of Pu have very different physical and chemical properties, it is critical that Pu metal be homogenous in phase to ensure that the metal properties are uniform. In conclusion, this novel surface analysis investigation concluded that the HH-LIBS device can be used to determine important information about the alloy production process and quantitatively assess the quality of the alloy.

5. Conclusion

This proof-of-concept study demonstrated plutonium surrogate detection and quantitative analysis capabilities of the commercially available Z500-ER HH-LIBS device. Previous efforts demonstrated this capability only for uranium compounds and rare earth metals. [17, 18]. A standard benchtop LIBS system lacks portability and speed needed for rapid in-situ impurity measurements. In this research, the portable Z500 system was coupled with chemometric techniques to develop the means to rapidly detect Pu surrogate metal and quantify gallium concentrations in the metal alloy. The development of these data collection and analysis techniques lays groundwork for developing calibration and detection programs which can provide quick and accurate measurements of plutonium alloys.

To investigate basic dopant concentration analysis, univariate calibration curves are created using 4 different emission lines of Ga and Ce identified through prior analysis of different cerium and gallium samples. Limits of detection are calculated to quantitatively compare the different calibrations; the calibration curves using the Ga I 287.4 nm line are determined to yield superior LODs and univariate calibration models. Next, comparisons between different multivariate analysis models investigate the performance of more advanced chemometric techniques in analyzing the cerium alloy. A simple multivariate linear regression is shown to yield better LODs than all of the univariate calibration curves analyzed initially. Principle components analysis was conducted on the emission spectra for purposes of dimensionality reduction. The PCA coefficients of the decomposed latent variables allowed for the identification of several significantly varying emissions in the Ce-Ga alloy spectra. From these selected emissions, elemental clustering capabilities were demonstrated by plotting the loadings values of different principal components. It is determined that PCA can separate emission wavelength variables based on upper energy level designations

and their electronic structure. Scores comparisons of different principle components are shown to cluster the sample set based on outcome values; Rotating a 3D plot of the scores of the first three PCs showed different patterns grouping the samples based on Ga concentration. Finally, predictive calibration models using PCA and PLS are compared. While both PCR and PLSR demonstrated the capabilities to sort the sample set based on Ga concentration, the PLS regression produced the superior fitted model to the data set. This is due to the fact that PLS latent variables explain variance in both the predictor and outcome variable set, while PCR only explains variance in the predictor. As a result, the R^2 and RMSECV values of the PLSR model were superior to those of the PCR model, and it was determined that a PLSR routine would be most useful to create a Pu analysis program for the Z500's onboard computer. These results yielded several important conclusions for the further progression of the Pu alloy analysis project.

The Z500-ER shows great promise in being able to assist in delivering the rapid, portable analysis tool needed for in-situ analysis of Pu metal during the production process. Conducting this extensive study on the cerium alloys allowed for the refining of the data collection process needed to gather usable spectra of Pu alloys. Additionally, investigating the plethora of analysis techniques discussed in this thesis work determined the best chemometric techniques to use in order to analyze impurities in the Pu alloy metal. Future work will build on the processes and analytical techniques refined in this study to conduct a thorough analysis of Pu samples.

5.1 Dissertation Research

This work provided an essential component for advancing the development of a program to quantitatively analyze Pu alloys using the Z500-ER. However, further work is required to improve all aspects of this on-going project related to analyzing

the complex plutonium spectra using the techniques investigated in this Master's thesis. Further research areas for investigation include:

- **Improving the PLSR model with a larger data set and performing several rounds of training, validation and testing.** This is critical to refining this multivariate technique and applying it to the analysis of more complex spectra. This would culminate in the development of an automated PLSR routine which could be coupled to the HH-LIBS device.

- **Investigate even more advanced analytical techniques to sort through a large set of spectra and identify similarities and trends in the data.** Most likely, this would involve integrating machine learning capabilities into this project and processing spectra data sets of Pu with different types of neural networks. Cognitive and Deep Tensor Neural Networks could be easily programmed into the onboard computer of the Z500 and trained to analyze the plutonium spectral emissions. Other machine learning-based techniques, such as decision trees will also be investigated.

- **Investigate other impurities which can be introduced into the Pu chemical matrix during manufacture and processing.** Metal elements such as iron, aluminium, and silicon can be introduced into the Pu metal at several stages during the manufacturing process and are found in Pu samples taken for mass spec analysis. Identifying concentrations of these impurities at various stages in Pu production is critical to ensuring quality of the Pu metal. The MVA and machine learning techniques can be built to rapidly identify and determine concentrations of multiple elements from the same spectra.

- **Investigate the build-up of decay products in the plutonium metal due to aging.** Since Ce is not radioactive, this could not be done with the

current study presented. Particularly, we would like to investigate the Z500's ability to detect americium and uranium build up in the Pu metal over time in order to determine if the device can yield accurate chronometric measurements. Since the build up of decay products can change the interaction cross sections of the metal, it is critical that the pit production program have the ability to detect and monitor decay product ingrowth as the Pu metal ages.

- **Additional comparisons of HH-LIBS vs. HH-XRF to compare surface distribution mapping capabilities of both techniques on Ce-Ga and/or Pu-Ga alloys.** While this thesis briefly contrasted these two spectral analysis techniques, it would be highly beneficial to apply both to analysis of Pu samples and visually compare their performance in mapping surface concentration of the various dopant elements.

Bibliography

1. Office of the Secretary of Defense, "2018 Nuclear Posture Review," 2018.

2. P. S. Hsu, M. Gragston, Y. Wu, Z. Zhang, A. K. Patnaik, J. Kiefer, S. Roy, and J. R. Gord, "Sensitivity, stability, and precision of quantitative Ns-LIBS-based fuel-air-ratio measurements for methane-air flames at 1–11 bar," *Appl. Opt.*, vol. 55, no. 28, pp. 8042–8048, Oct 2016.

3. A. K. Patnaik, Y. Wu, P. S. Hsu, M. Gragston, Z. Zhang, J. R. Gord, and S. Roy, "Simultaneous LIBS signal and plasma density measurement for quantitative insight into signal instability at elevated pressure," *Opt. Express*, vol. 26, no. 20, pp. 25 750–25 760, Oct 2018.

4. M. L. Najarian and R. C. Chinni, "Temperature and Electron Density Determination on Laser-Induced Breakdown Spectroscopy (LIBS) Plasmas: A Physical Chemistry Experiment," *Journal of Chemical Education*, vol. 90, pp. 244–247, 2013.

5. L. Pardini, S. Legnaioli, G. Lorenzetti, V. Palleschi, R. Gaudiuso, A. D. Giacomo, D. D. Pace, F. A. Garcia, G. de Holanda Cavalcanti, and C. Parigger, "On the determination of plasma electron number density from Stark broadened hydrogen Balmer series lines in Laser-Induced Breakdown Spectroscopy experiments," *Spectrochimica Acta Part B: Atomic Spectroscopy*, vol. 88, pp. 98 – 103, 2013.

6. U. et al, "Measurements of plasma temperature and electron density in laser-induced copper plasma by time-resolved spectroscopy of neutral atom and ion emissions," *Pramana Journal of Physics*, vol. 74, pp. 983–993, 2010.

7. B. Bhatt, K. Hudson Angeyo, and A. Dehayem-Kamadjeu, "Libs development methodology for forensic nuclear materials analysis," *Anal. Methods*, vol. 10, pp. 791–798, 2018.

8. J. E. Barefield, E. J. Judge, K. R. Campbell, J. P. Colgan, D. P. Kilcrease, H. M. Johns, R. C. Wiens, R. E. Mcinroy, R. K. Martinez, and S. M. Clegg, "Analysis of geological materials containing uranium using laser-induced breakdown spectroscopy," *Spectrochim. Acta B*, vol. 120, pp. 1–8, 2016.

9. J. Klus, P. Mikysek, D. Prochazka, P. Porizka, P. Prochazkov, T. T. J. Novotny and, M. S. K. Novotny and, and J. Kaiser, "Multivariate approach to the chemical mapping of uranium in sandstone-hosted uranium ores analyzed using double pulse laser-induced breakdown spectroscopy," *Spectrochim. Acta B*, vol. 123, pp. 143–149, 2016.

10. J. Sirven, A. Pailloux, Y. Baye, N. Coulon, T. Alpettaz, and S. Gosse, "Towards the determination of the geographical origin of yellow cake samples by laser-induced breakdown spectroscopy and chemometrics," *J. Anal. At. Spectrom.*, vol. 24, pp. 451–459, 2009.

11. Y. Kim, B. Han, H. S. Shin, H. D. Kim, E. C. Jung, J. H. Jung, , and S. H. Na, "Determination of uranium concentration in an ore sample using laser-induced breakdown spectroscopy," *Spectrochim. Acta B*, vol. 75, pp. 190–193, 2012.

12. M. B. Shattan, M. Gragston, Z. Zhang, I. John D. Auxier, K. G. McIntosh, and C. G. Parigger, "Mapping of Uranium in Surrogate Nuclear Debris Using Laser-Induced Breakdown Spectroscopy (LIBS)," *Applied Spectroscopy*, vol. 73, no. 6, pp. 591–600, 2019.

13. R. Chinni, D. A. Cremers, and R. Multari, "Analysis of material collected on swipes using laser-induced breakdown spectroscopy," *Appl. Opt.*, vol. 49, pp. C143–C152, 2010.

14. D. A. A. Sarkar and S. K. Aggarwal, "Determination of thorium and uranium in solution by laser-induced breakdown spectrometry," *Appl. Opt.*, vol. 4, pp. G58–G64, 2008.

15. I. Gaona, J. Serrano, J. Moros, and J. J. Laserna, "Evaluation of laser-induced breakdown spectroscopy analysis potential for addressing radiological threats from a distance," *Spectrochim. Acta B*, vol. 96, pp. 12–20, 2014.

16. SciAps. (2019) LIBS Analyzer Models. [Online]. Available: https://www.sciaps.com/libs-handheld-laser-analyzers/z-series/

17. M. B. Shattan, D. J. Miller, M. T. Cook, A. C. Stowe, J. D. Auxier, C. Parigger, and H. L. Hall, "Detection of uranyl fluoride and sand surface contamination on metal substrates by hand-held laser-induced breakdown spectroscopy," *Appl. Opt.*, vol. 56, no. 36, pp. 9868–9875, Dec 2017.

18. B. T. Manard, E. M. Wylie, and S. P. Wilson, "Analysis of Rare Earth Elements in Uranium Using Handheld Laser-Induced Breakdown Spectroscopy (HH LIBS)," *Applied Spectroscopy*, vol. 72, no. 11, pp. 1653–1660, 2018.

19. E. Judge, J. M. Berg, L. A. Le, L. N. Lopez, and J. E. Barefield, "LIBS Spectral Data for a Mixed Actinide Fuel Pellet Containing Uranium, Plutonium, Neptunium and Americium," 2012.

20. G. L. Donati, R. S. Amais, and C. B. Williams, "Recent advances in inductively coupled plasma optical emission spectrometry," *J. Anal. At. Spectrom.*, vol. 32, pp. 1283–1296, 2017.

21. M. Krachler and R. Alvarez-Sarandes, "Capabilities of high resolution ICP-OES for plutonium isotopic analysis," *Microchemical Journal*, vol. 125, pp. 196 – 202, 2016.

22. M. Moore and Y. Tao, "Aerosol physics considerations for using cerium oxide ceo2 as a surrogate for plutonium oxide puo2 in airborne release fraction measurements for storage container investigations," 2017.

23. H. Zheng, F.-Y. Yueh, T. Miller, J. Singh, K. E. Zeigler, and J. C. Marra, "Analysis of plutonium oxide surrogate residue using laser-induced breakdown spectroscopy," *Spectrochimica Acta*, vol. 63, pp. 968–974, 2008.

24. F. E. Gibbs, D. L. Olson, and W. Hutchinson, "Identification of a physical metallurgy surrogate for the plutonium1 wt.% gallium alloy," *AIP Conference Proceedings*, vol. 532, no. 1, pp. 98–101, 2000.

25. C. Dowding, "19 - laser ablation," in *Advances in Laser Materials Processing*, ser. Woodhead Publishing Series in Welding and Other Joining Technologies, J. Lawrence, J. Pou, D. Low, and E. Toyserkani, Eds. Woodhead Publishing, 2010, pp. 575 – 628.

26. H. Hu, X. Wang, and H. Zhai, "High-fluence femtosecond laser ablation of silica glass: effects of laser-induced pressure," *Journal of Physics D: Applied Physics*, vol. 44, no. 13, p. 135202, mar 2011.

27. U. Fantz, "Basics of plasma spectroscopy," *Plasma Sources Science and Technology*, vol. 15, no. 4, pp. S137–S147, oct 2006.

28. H. Griem, *Spectral Line Broadening by Plasmas*. New York: Academic Press, 1974.

29. S. Zhang, X. Wang, M. He, Y. Jiang, B. Zhang, W. Hang, and B. Huang, "Laser-induced plasma temperature," *Spectrochimica Acta Part B: Atomic Spectroscopy*, vol. 97, pp. 13 – 33, 2014.

30. G. Cristoforetti, M. Aglio, and S. Legnaioli, "Local thermodynamic equilibrium in laser-induced breakdown spectroscopy: Beyond the McWhirter criterion beyond the McWhirter criterion," *Spectrochim. Acta Part B*, vol. 65, pp. 86–95, 01 2009.

31. M. S. et al, "Determination of deuterium depth profiles in fusion-relevant wall materials by nanosecond libs," *Nuclear Materials and Energgy*, vol. 12, pp. 611 – 616, 2017.

32. M. A. Gondal, Y. W. Maganda, M. A. Dastageer, F. F. Al-Adel, and A. Naqvi, "Study of temporal evolution of electron density and temperature for atmospheric plasma generated from fluid samples using laser induced breakdown spectroscopy," in *2013 Saudi International Electronics, Communications and Photonics Conference*, April 2013, pp. 1–4.

33. A. Kramida, Y. Ralchenko, and J. Reader, "NIST Atomic Spectra Database." [Online]. Available: https://physics.nist.gov/asd

34. A. P. Rao, M. Gragston, A. K. Patnaik, P. S. Hsu, and M. B. Shattan, "Measurement of electron density and temperature from laser-induced nitrogen plasma at elevated pressure," *Opt. Express*, vol. 27, no. 23, pp. 33 779–33 788, Nov 2019.

35. D. Hahn and N. Omenetto, "Laser-Induced Breakdown Spectroscopy (LIBS), Part I: Review of Basic Diagnostics and Plasma-Particle Interactions: Still-Challenging Issues Within the Analytical Plasma Community," *Applied Spectroscopy*, vol. 64, pp. 335–66, 12 2010.

36. H. Griem, *Plasma Spectroscopy.* New York: McGraw-Hill, 1964.

37. H.Griem, *Principles of Plasma Spectroscopy.* New York: McGraw-Hill, 1997.

38. Z. Cong, L. Sun, Y. Xin, Y. Li, and L. Qi, "Comparison of Calibration Curve Method and Partial Least Square Method in the Laser Induced Breakdown Spectroscopy Quantitative Analysis," *Journal of Computer and Communications*, vol. 1, pp. 14–18, 2013.

39. D. W. Hahn and N. Omenetto, "laser-induced breakdown spectroscopy (libs), part ii: Review of instrumental and methodological approaches to material analysis and applications to different fields," *Appl. Spectrosc.*, no. 4, pp. 347–419.

40. R. Noll, V. Sturm, mit Aydin, D. Eilers, C. Gehlen, M. Hhne, A. Lamott, J. Makowe, and J. Vrenegor, "Laser-induced breakdown spectroscopyfrom research to industry, new frontiers for process control," *Spectrochimica Acta Part B: Atomic Spectroscopy*, vol. 63, no. 10, pp. 1159 – 1166, 2008.

41. Radboud, "General instrumentation," https://www.ru.nl/science/gi/facilities-activities/elemental-analysis/icp-oes/, Dec 2018, accessed on 2019-04-16.

42. J. Patterson, "HH-XRF and HH-LIBS for alloy analysis Choosing the Right Tool for the Right Job," 2014.

43. SciAps, "LIBS vs. X-Ray," 2019. [Online]. Available: https://www.sciaps.com/libs-vs-x-ray-the-whole-story/

44. P. Soderlind, F. Zhou, A. Landa, and J. Klepeis, "Phonon and magnetic structure in -plutonium from density-functional theory," *Scientific Reports*, vol. 5, p. 15958, 10 2015.

45. S. S. Hecker, "Plutonium: Coping with instability," *JOM*, vol. 55, no. 9, pp. 13–19, Sep 2003.

46. M. Steinzig and F. H. Harlow, "Characterization of cast metals with probability distribution functions," *MRS Proceedings*, vol. 538, 03 1999.

47. J. Marra, "Cerium as a surrogate in the plutonium immobilized form," 6 2001.

48. J. L. Bishop, "Hand held LIBS analysis of Post Detonation Synthetic Nuclear Melt Glass," *American Chemical Society Fall National Meeting*, 2019.

49. J. Gruber, J. Heitz, N. Arnold, D. Buerle, N. Ramaseder, W. Meyer, J. Hochrtler, and F. Koch, "In situ analysis of metal melts in metallurgic vacuum devices by laser-induced breakdown spectroscopy," *Applied Spectroscopy*, vol. 58, no. 4, pp. 457–462, 2004.

50. G. Guo, G. Niu, Q. Shi, Q. Lin, D. Tian, and Y. Duan, "Multi-element quantitative analysis of soils by laser induced breakdown spectroscopy (libs) coupled with univariate and multivariate regression methods," *Anal. Methods*, vol. 11, pp. 3006–3013, 2019.

51. J. L. Gottfried, R. S. Harmon, F. C. D. Lucia, and A. W. Miziolek, "Multivariate analysis of laser-induced breakdown spectroscopy chemical signatures for geomaterial classification," *Spectrochim Acta B*, vol. 64, no. 10, pp. 1009 – 1019, 2009.

52. P. K. Tiwari, S. Awasthi, R. Kumar, R. K. Anand, P. K. Rai, and A. K. Rai, "Rapid analysis of pharmaceutical drugs using libs coupled with multivariate analysis," *Lasers in Medical Science*, vol. 33, no. 2, pp. 263–270, Feb 2018.

53. C. R. Bhatt, F. Y. Yueh, and J. P. Singh, "Univariate and multivariate analyses of rare earth elements by laser-induced breakdown spectroscopy," *Appl. Opt.*, vol. 56, no. 8, pp. 2280–2287, Mar 2017.

54. S. M. Clegg, E. Sklute, M. D. Dyar, J. E. Barefield, and R. C. Wiens, "Multivariate analysis of remote laser-induced breakdown spectroscopy spectra using partial least squares, principal component analysis, and related techniques," *Spectrochimica Acta Part B: Atomic Spectroscopy*, vol. 64, no. 1, pp. 79 – 88, 2009.

55. D. Larose and C. Larose, *Data Mining and Predictive Analysis*. Wiley, 2015.

56. R. P. Menon, "Data science simplified part 5: Multivariate regression models," Aug 2017. [Online]. Available: https://towardsdatascience.com/data-science-simplified-part-5-multivariate-regression-models-7684b0489015

57. N. Yang, N. Eash, J. Lee, M. Martin, Y.-S. Zhang, F. Walker, and J. E. Yang, "Multivariate analysis of laser-induced breakdown spectroscopy spectra of soil samples," *Soil Science*, vol. 175, pp. 447–452, 09 2010.

58. Z. Jaadi, "A step by step explanation of principal component analysis," May 2019. [Online]. Available: https://towardsdatascience.com/a-step-by-step-explanation-of-principal-component-analysis-b836fb9c97e2

59. P. Porizka, "Using laser-induced breakdown spectroscopy (libs) for material analysis," 2014.

60. Www.statsoft.com, "Partial least squares (pls)." [Online]. Available: http://www.statsoft.com/Textbook/Partial-Least-Squares

61. P. Geladi and B. Kowalski, "Partial-least squares regression: A tutorial," *Analytica Chimica Acta*, vol. 185, pp. 1–17, 1986.

62. Mathworks.com, "Partial least squares regression and principal components regression - matlab and simulink example." [Online]. Available: https://www.mathworks.com/help/stats/examples/partial-least-squares-regression-and-principal-components-regression.html

63. SciAps, "SciAps Z Brochure," 2014. [Online]. Available: https://www.sciaps.com/wp-content/uploads/2014/08/Z-brochureRGB.pdf

64. D. M. Surmick and C. G. Parigger, "Empirical formulae for Electron Density Diagnostics from H_α and H_β Line Profiles," *IRAMP*, vol. 5, no. 2, pp. 73–81, July 2014.

65. A. Rao, M. Cook, H. Hall, and M. Shattan, "Quantitative analysis of cerium-gallium alloys using a hand-held laser-induced breakdown spectroscopy device." *Atoms*, vol. 84, no. 7, 2019.

Vita

2d Lt Rao was born and raised in San Diego, CA. He received his undergraduate degree from the University of Michigan, where graduated Summa Cum Laude with a B.S.E. Nuclear Engineering and Radiological Sciences in April 2018. He also earned his commission in April 2018 from AFROTC Detachment 390. Prior to entering active duty, 2d Lt Rao worked as an undergraduate research assistant in the Michigan Plasma, Pulsed Power, and Microwave Lab, supporting research on Z-pinches. He assisted in the development of a new conical power feed as well as the design of new diagnostic hardware for the Michigan Accelerator for Inductive Z-pinch Experiments (MAIZE). He also worked as an intern in the Pulsed Power Technology R+D Division of Sandia National Laboratories in 2016 and 2017, where he assisted with research supporting the development of radiographic accelerators and diagnostic systems for the Z-machine.

2d Lt Rao has been stationed at WPAFB, OH since May 2018 and is pursuing graduate degrees in Nuclear Engineering at the Air Force Institute of Technology. His research mainly focuses on nuclear applications of laser-induced breakdown spectroscopy (LIBS), but also includes investigating LIBS for combustion/plasma diagnostics as well as image processing techniques for analysis of digitized nuclear detonation test films.

REPORT DOCUMENTATION PAGE

Form Approved
OMB No. 0704–0188

1. REPORT DATE *(DD–MM–YYYY)*	2. REPORT TYPE	3. DATES COVERED *(From — To)*
26–03–2020	Master's Thesis	Jun 2018 — Mar 2020

4. TITLE AND SUBTITLE

Rapid Analysis of Plutonium Surrogate Material via Hand-held Laser-induced Breakdown Spectroscopy

5a. CONTRACT NUMBER

5b. GRANT NUMBER

5c. PROGRAM ELEMENT NUMBER

6. AUTHOR(S)

Rao, Ashwin P, 2d Lt, USAF

5d. PROJECT NUMBER

5e. TASK NUMBER

5f. WORK UNIT NUMBER

7. PERFORMING ORGANIZATION NAME(S) AND ADDRESS(ES)

Air Force Institute of Technology
Graduate School of Engineering and Management (AFIT/EN)
2950 Hobson Way
WPAFB OH 45433-7765

8. PERFORMING ORGANIZATION REPORT NUMBER

AFIT-ENP-MS-20-M-115

9. SPONSORING / MONITORING AGENCY NAME(S) AND ADDRESS(ES)

Air Force Technical Applications Center, Patrick AFB, FL
Air Force Office of Scientific Research, WPAFB, OH
Defense Threat Reduction Agency, Ft. Belvoir, VA
Department of Homeland Security
Los Alamos National Laboratory, Los Alamos, NM

10. SPONSOR/MONITOR'S ACRONYM(S)

AFTAC, AFOSR, DTRA, DHS, LANL

11. SPONSOR/MONITOR'S REPORT NUMBER(S)

12. DISTRIBUTION / AVAILABILITY STATEMENT

APPROVED FOR PUBLIC RELEASE; DISTRIBUTION A: UNLIMITED.

13. SUPPLEMENTARY NOTES

14. ABSTRACT

This work investigated the capability of a portable LIBS device to detect and quantify dopants in plutonium surrogate alloys, specifically gallium, which is a common stabilizer used in plutonium alloys. The SciAps Z500-ER was utilized to collect spectral data from cerium-gallium alloys of varying gallium concentrations. Calibration models were built to process spectra from the Ce-Ga alloys and calculate gallium concentration from spectral emission intensities. Univariate and multivariate analysis techniques were used to determine limits of detection of different emission line ratios. Spatial mapping measurements were conducted to determine the device's ability to detect variations in gallium concentration on the surface of sample. Chemometric techniques were implemented to build predictive calibration models from the entire spectral data set. Partial least-squares regression was determined to produce the superior calibration model for predicting Ga content in a Ce-Ga alloy. The results demonstrated the SciAps Z500-ER can be coupled with advanced multivariate analytical routines to efficiently and rapidly provide quantitative analysis of impurities in plutonium surrogate metal. By using a handheld LIBS device in lieu of traditional mass spectrometry methods, the chemical analysis time can be reduced to mere seconds. This has direct applications for several national security applications including directly enabling Pu pit production teams to meet the 80 pit-per-year production goal outlined in the 2018 Nuclear Posture Review among others.

15. SUBJECT TERMS

LIBS, cerium, plutonium, laser-induced breakdown spectroscopy, plasma spectroscopy, chemometrics

16. SECURITY CLASSIFICATION OF:			17. LIMITATION OF ABSTRACT	18. NUMBER OF PAGES	19a. NAME OF RESPONSIBLE PERSON
a. REPORT	b. ABSTRACT	c. THIS PAGE			LTC Michael B. Shattan, AFIT/ENP
U	U	U	UU	103	19b. TELEPHONE NUMBER *(include area code)* (937) 255-3636, x4587